minerals

MDPI

Article

Pyrite Varieties at Pobeda Hydrothermal Fields, Mid-Atlantic Ridge 17°07′–17°08′ N: LA-ICP-MS Data Deciphering

Valeriy V. Maslennikov [1], Georgy Cherkashov [2], Dmitry A. Artemyev [1], Anna Firstova [2], Ross R. Large [3], Aleksandr Tseluyko [1,*] and Vasiliy Kotlyarov [1]

1 Institute of Mineralogy South, Urals Research Center of Mineralogy and Geoecology of the Urals Branch of the Russian Academy of Sciences, Ilmeny Reserve, 456317 Miass, Russia; mas@mineralogy.ru (V.V.M.); daartemyev@gmail.com (D.A.A.); kotlyarov@mineralogy.ru (V.K.)

2 Institute for Geology and Mineral Resources of the Ocean (FSBI "VNIIOkeangeologia"), Angliisky Ave, 1, 190121 St. Petersburg, Russia; gcherkashov@gmail.com (G.C.); anetfirst@gmail.com (A.F.)

3 CODES Centre for Ore Deposits and Earth Sciences, Private Bag 79, University of Tasmania, Tasmania 7001, Australia; Ross.Large@utas.edu.au

* Correspondence: faenarus@gmail.com

Received: 28 April 2020; Accepted: 7 July 2020; Published: 12 July 2020

Abstract: The massive sulfide ores of the Pobeda hydrothermal fields are grouped into five main mineral microfacies: (1) isocubanite-pyrite, (2) pyrite-wurtzite-isocubanite, (3) pyrite with minor isocubanite and wurtzite-sphalerite microinclusions, (4) pyrite-rich with framboidal pyrite, and (5) marcasite-pyrite. This sequence reflects the transition from feeder zone facies to seafloor diffuser facies. Spongy, framboidal, and fine-grained pyrite varieties replaced pyrrhotite, greigite, and mackinawite "precursors". The later coarse and fine banding oscillatory-zoned pyrite and marcasite crystals are overgrown or replaced by unzoned subhedral and euhedral pyrite. In the microfacies range, the amount of isocubanite, wurtzite, unzoned euhedral pyrite decreases versus an increasing portion of framboidal, fine-grained, and spongy pyrite and also marcasite and its colloform and radial varieties. The trace element characteristics of massive sulfides of Pobeda seafloor massive sulfide (SMS) deposit are subdivided into four associations: (1) high temperature—Cu, Se, Te, Bi, Co, and Ni; (2) mid temperature—Zn, As, Sb, and Sn; (3) low temperature—Pb, Sb, Ag, Bi, Au, Tl, and Mn; and (4) seawater—U, V, Mo, and Ni. The high contents of Cu, Co, Se, Bi, Te, and values of Co/Ni ratios decrease in the range from unzoned euhedral pyrite to oscillatory-zoned and framboidal pyrite, as well as to colloform and crystalline marcasite. The trend of Co/Ni values indicates a change from hydrothermal to hydrothermal-diagenetic crystallization of the pyrite. The concentrations of Zn, As, Sb, Pb, Ag, and Tl, as commonly observed in pyrite formed from mid- and low-temperature fluids, decline with increasing crystal size of pyrite and marcasite. Coarse oscillatory-zoned pyrite crystals contain elevated Mn compared to unzoned euhedral varieties. Framboidal pyrite hosts maximum concentrations of Mo, U, and V probably derived from ocean water mixed with hydrothermal fluids. In the Pobeda SMS deposit, the position of microfacies changes from the black smoker feeder zone at the base of the ore body, to seafloor marcasite-pyrite from diffuser fragments in sulfide breccias. We suggest that the temperatures of mineralization decreased in the same direction and determined the zonal character of deposit.

Keywords: pyrite; microfacies; minerals; trace elements; LA-ICP-MS; Mid-Atlantic Ridge; Pobeda hydrothermal field; massive sulfide deposits

1. Introduction

The analysis of trace element (TE) contents in different generations of pyrite by use of high-resolution laser ablation inductively-coupled plasma mass spectrometry (LA-ICP-MS) has aided constructions of ore deposits models and helped to solve conjecture related to ore genesis [1–9] and paleoocean geochemical features [10].

The best results were obtained when LA-ICP-MS analyses were combined with genetic interpretation of mineral microfacies and facies [11–28]. Most studies so far were dedicated to black smoker chimney microfacies, and less is known about trace elements partitioning in sulfides of low-temperature hydrothermal pyrite-rich crusts associated with diffusers in comparison with high-temperature black smoker microfacies [26]. Limited data can be found on seafloor massive sulfide (SMS) deposits hosted by ultramafic–mafic rock sequences [17,18,21].

In this paper, we investigate mineral microfacies of portions of massive sulfides or sulfide-bearing deposits at the mafic–ultramafic-hosted Pobeda hydrothermal field, Mid-Atlantic Ridge. Special microtextural, mineral, and geochemical features are shown to reflect conditions of the mineralization processes. Microtextures are visible and identifiable only under the transmitted or reflected light microscope at low magnification [29,30]. The microfacies are defined by the coeval microtextural, mineral species, geochemical characteristics, temperature, redox-potential, and other changes in the construction of the sulfide deposits.

The initial step is documentation of pyrite varieties in each microfacies, followed by analysis to determine the concentrations and nature of trace elements in the host minerals (e.g., contained in solid solution, present as submicroscopic mineral inclusions, or adsorbed onto sulfide surfaces as micrograins of minerals). This leads on to the critical understanding of the spatial evolution of morphogenetic and zonation features of pyrite and also crystal sizes with their trace element characteristics. The target of the current research is assessment of the processes for trace element enrichment and partitioning in different varieties of pyrite and their microfacies.

2. Geological Setting

The Pobeda massive sulfide hydrothermal field was discovered on the eastern flank of the Mid-Atlantic Ridge rift valley (17°08′ N) (Figure 1) during for 37th cruise (2014–2015) of the Russian R.V. Professor Logatchev by the Polar Marine Geosurvey Expedition (PMGE) in collaboration with VNIIOkeangeologia, Saint-Petersburg, Russia [31,32]. The Pobeda SMS deposit is located on the western slope of an oceanic core complex at depths between 1950 and 3100 m. The host rocks are composed of serpentinized peridotites, serpentinites, gabbros, basalts, and dolerite dykes [33]. The hydrothermal SMS deposit consists of the Pobeda-1 and Pobeda-2 hydrothermal fields and the Pobeda-3 sulfide occurrence (Figure 1).

The active hydrothermal field Pobeda-1 (17°08′7″ N, 46°23′44″ W) is located at water depths between 1950 and 2400 m. It consists of four sulfide bodies, some gossanous ferruginous crusts, and metalliferous sediments. The sulfide bodies are sulfide mounds about 10 m in height, some of which are sulfide chimneys and fragments of sulfide chimneys and diffusers. The active Pobeda-2 hydrothermal field (17°07′45″ N, 46°24′5″ W) is situated 4 km southwest of the Pobeda-1 at water depths between 2800 and 3100 m. Similar to the Pobeda-1, the Pobeda-2 is associated with peridotites and gabbronorites. The Pobeda-3 (17°08′3″ N, 46°25′2″ W) is located at the depth of 2500 to 2700 m and mostly covered by metalliferous sediments with Fe–Mn crusts, pyrite, and barite grains [34].

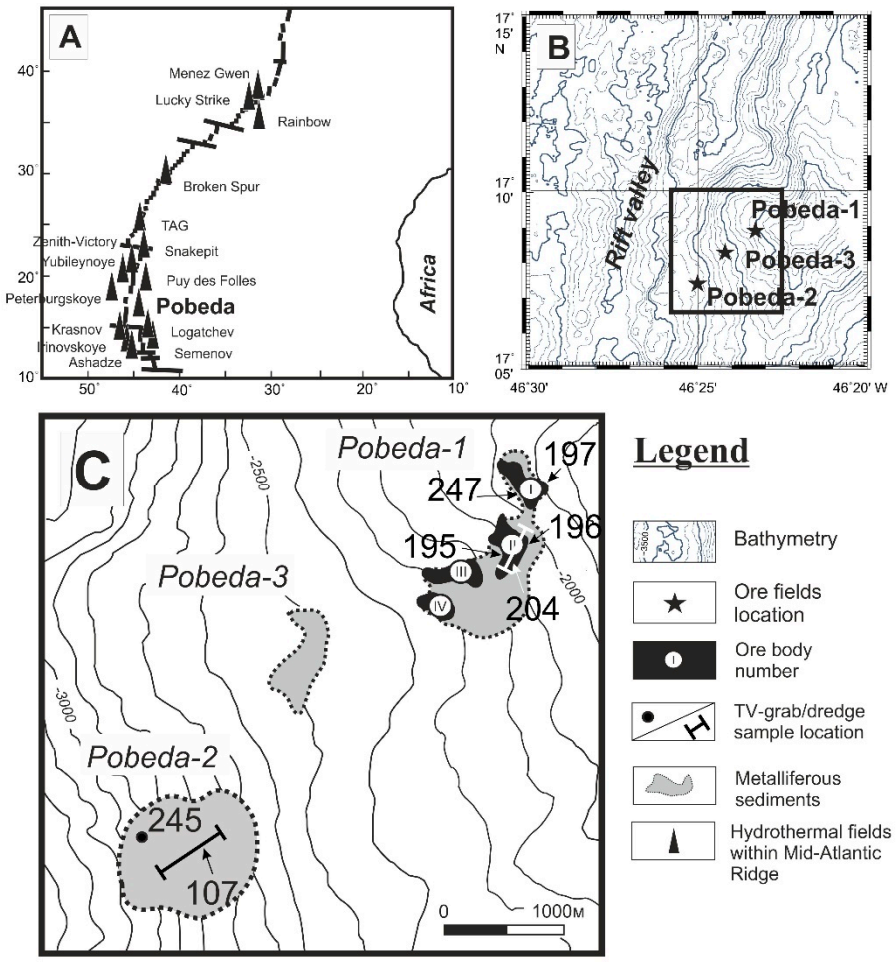

Figure 1. Geological setting of the Pobeda massive sulfide hydrothermal cluster. (**A**) Location of the Pobeda cluster at the Mid-Atlantic Ridge; (**B**) The Pobeda -1, 2 and 3 hydrothermal fields at the Mid-Atlantic Ridge bathymetry; (**C**) Detailed scheme of hydrothermal fields with the sampling station locations.

3. Materials and Methods

The ore materials were obtained with the TV-grab and dredge [31,32]. Samples 37L195-2, 37L196a, and 37L204d-OB were taken from the sulfide body II from the hydrothermal field Pobeda-1. Samples 37L107d-1,2 and 37L107-10 were taken from the hydrothermal field Pobeda-2 (Figure 1). The morphogenetic types and general mineral composition of the samples were previously described [34,35].

All samples have been studied by use of reflected light microscopy. The surfaces of some sulfides have been etched by concentrated HNO_3 mixed with CaF_2 powder. Microinclusions of minerals in pyrite were identified by using a Vega-3 SBU TESCAN SEM (Tescan, Brno, Czech Republic) and a REMMA–2M SEM (Sumy factory of electron microscopes, Sumy, USSR) equipped with a Link LZ-5 ED system at the Institute of Mineralogy of the South Urals Federal Research Center of Mineralogy and Geoecology UB RAS.

Quantitative LA-ICP-MS analyses of trace elements (^{51}V, ^{52}Cr, ^{55}Mn, ^{59}Co, ^{60}Ni, ^{65}Cu, ^{66}Zn, ^{75}As, ^{77}Se, ^{95}Mo, ^{107}Ag, ^{111}Cd, ^{118}Sn, ^{121}Sb, ^{125}Te, ^{182}W, ^{197}Au, ^{205}Tl, ^{208}Pb, ^{209}Bi, ^{232}Th, and ^{238}U) were carried out on a New Wave 213-nm solid-state laser microprobe coupled to an Agilent 7700 quadrupole ICP-MS housed at the Federal Scientific Centre of UB RAS. The analyses were performed by ablating spots ranging in size from 35 to 60 μm. Laser repetition rate was 10 Hz, and laser beam energy at

the sample was maintained between 3 and 4 J/cm^2. The analysis time for each spot was 75–80 s, comprising a 20–30 s measurement of background (laser off) and a 45–60 s measurement with laser on. The mass-spectrometer was calibrated by use of multielemental solutions. The trace element contents were calculated in an Iolite program by use of international glass (BCR-2G and GSD-1G) and sulfide (MASS-1) standards and ^{57}Fe as the internal standard for quantification of pyrite (46.5%). Detection limits (DL) of the trace elements are much lower than obtained values, except for Au, Bi, and Te where DL are varied in the range of 0.01–0.1 and Se with DL of 0.1–1. In that case, if the value is below DL, we have to use half DL to complete statistical calculation.

The LA-ICP-MS data were processed in Statistica program v.10 by use of correlation analyses. The trace element associations were calculated by the method of "maximal correlation way" (MCW) [36]. The source material was half the square correlation matrix, in which, only statistically significant correlation coefficients were recorded. The maximum modulus of the correlation coefficients was ranged for each of the following element. A new selection was not made if the element with maximum correlation coefficients were selected previously. Several high associations were divided by minimum values of correlation coefficients.

We have to note that the scanning capability of LA-CP-MS cannot be used to distinguish between homogeneously distributed nanoinclusions and lattice-bound elements, since both types of trace metals may display flat concentration patterns [1,2,5,18]. Substitution could generally be inferred if the ionic radius of the two elements are similar. Significant variations in the trace metal contents with time would instead suggest mineral inclusions are present (e.g., [4,19]).

The following symbols are used for minerals in figures below: Bn, bornite; Chp, chalcopyrite; Ge, geerite; Grg, greigite; Iso, isocubanite; Ms, marcasite; Po, pyrrhotite; Py, pyrite; Sph, sphalerite; and Wtz, wurtzite.

4. Results

4.1. Isocubanite-Pyrite and Pyrite-Wurtzite-Isocubanite Crust Microfacies

Aggregates of subhedral crystals of isocubanite and chalcopyrite contain disseminated euhedral and subhedral pyrite. Their atoll-like microtexture (Figure 2a) were probably formed due to recrystallization of primary unstable fine-grained sulfides. Unzoned subhedral and euhedral pyrite crystals were encrusted on the walls of the microcavities (Figure 2b). Isocubanite crystals were complicated by lattice-controlled chalcopyrite lamellae. Relic pyrrhotite-$Fe_{0.9}S$ inclusions occurred in the isocubanite-chalcopyrite aggregates. The aggregates were replaced by covellite and geerite—(Cu_9S_5) with latest pyrite veinlets (Figure 2c).

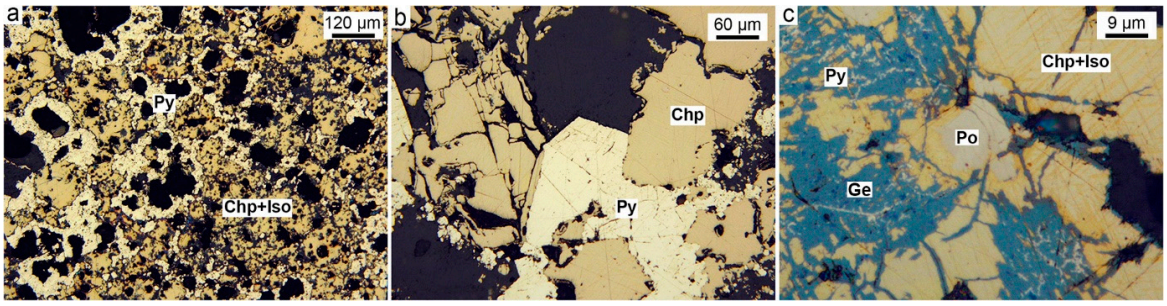

Figure 2. Isocubanite–pyrite microfacies. Pobeda-2 and Pobeda-1 hydrothermal fields. (**a**) Atoll-like aggregates of unzoned pyrite (Py) in chalcopyrite–isocubanite (Chp-Iso) aggregate (sample 107-2); (**b**) unzoned subhedral crystals of pyrite (Py) in the cavity of chalcopyrite–pyrite (Chp) aggregate (sample 204d-4); (**c**) inclusion of pyrrhotite (Po) in chalcopyrite–isocubanite (Chp-Iso) aggregate in association with geerite (Ge) and veinlets of the latest pyrite-related (Py) to the chalcopyrite alteration to geerite. Reflected light.

Pyrite-3 crystals have high contents of Co, Ni, and Se. The contents of As and Sb as well as Mn, Tl, and Pb assemblages displayed low values (Table 1, Table S1, Figure 3). In comparison to isocubanite, pyrite-3 had much less Te and Se.

Table 1. Trace element contents in the pyrite-chalcopyrite crusts. Pobeda vent site. LA-ICP-MS data in ppm. Fe, Cu, Zn are in wt. %.

Values	V	Mn	Fe	Co	Ni	Cu	Zn	As	Se	Mo	Ag	Cd	Sn	Sb	Te	Au	Tl	Pb	Bi	U
Pyrite-3—coarse-grained subhedral to euhedral unzoned (n = 34)																				
Mean	2.6	4.7	45.6	2489	171	0.58	0.02	61	108	35	5.6	1.0	0.9	1.9	2.0	0.2	1.7	29	4.0	6.3
Std	2.0	12	0.7	1171	85	0.73	0.04	41	59	48	4.3	0.9	0.6	1.5	1.7	0.1	1.3	21	3.7	17
Max	7.8	65	46.4	5220	346	3.9	0.2	171	311	270	19	3.6	2.4	7.2	6.1	0.5	6.2	107	16	75
Med	2.1	1.4	45.8	2271	178	0.3	0.01	55	103	21	4.5	0.6	0.7	1.6	1.4	0.2	1.4	24	2.4	0.9
Isocubanite (+ chalcopyrite) (n = 47)																				
Mean	0.8	15	35	1954	65	23.3	0.25	15	700	41	10	9.3	26	1.3	33	0.3	2.0	48	3.8	2.8
Std	0.8	6.1	5	1402	231	4.1	0.24	20	602	192	6.0	5.4	26	2.7	43	0.3	5.6	101	7.2	17
Max	3.7	36	41	11100	1580	38.6	1.63	70	2000	1250	30	22	81	18	184	2.2	29	525	38	116
Med	0.7	15	36.9	1636	15	23.3	0.2	6	490	0.9	10	9	10	0.5	14	0.3	0.3	6.2	1.3	0.1

Std, standard deviation; Max, maximum; Med, median.

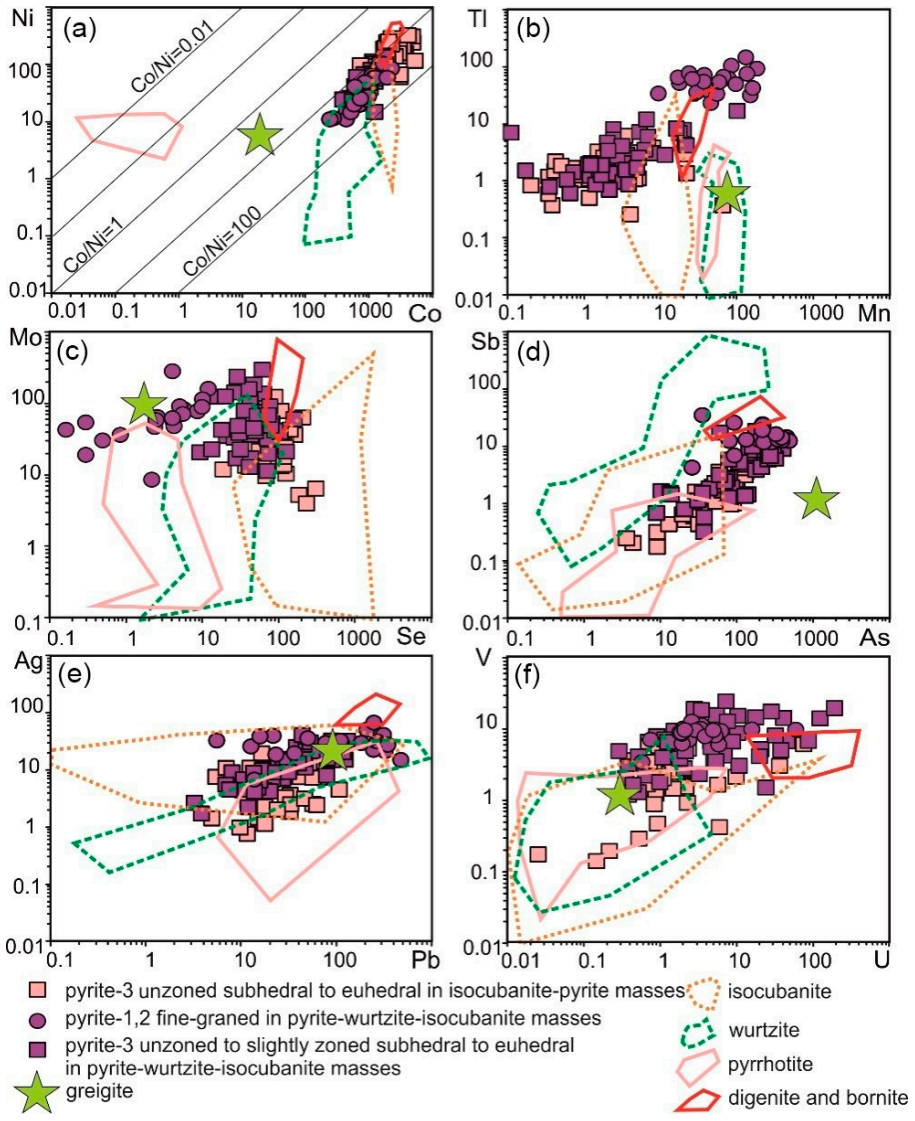

Figure 3. Diagrams showing trace element concentrations in sulfides from isocubanite-pyrite (pink) and pyrite-wurtzite-isocubanite (purple) microfacies. (**a**) Co vs Ni ratio; (**b**) Mn vs Tl ratio; (**c**) Se vs Mo ratio; (**d**) As vs Sb ratio; (**e**) Pb vs Ag ratio; (**f**) U vs V ratio.

The distribution of most pyrite-3 plotted points was similar to isocubanite in several diagrams (Figure 3). The exception was Ni with higher concentration in pyrite-3 as well as in submarine supergene bornite and digenite as opposed to isocubanite (Figure 3a). The contents U, V, and Mo were commonly low or variable in pyrite-3 and isocubanite (Table 1).

The series of diagrams exhibited the most important positive relationships of elements: Co-Ni, Mn-Tl, Sb-As, Ag-Pb, and V-U (Figure 3a,b,d–f) versus negative correlation of Se and Mo (Figure 3c).

Calculation by methods of MCW [36] showed the following series of mineral and chemical assemblages: I(V + Sb + As) + II(Pb + Bi + Au + Ag) + Cd + III(Cu + U + Mo + Te) − IV(Sn + Zn + Tl) − V(Ni + Co + Se) − Mn. The association (I) could likely be related to invisible inclusions of tennantite in pyrite. The second association is typical for the assemblage with native gold and galena inclusions in terms of the well-known substitution: $2Pb^{2+} = Bi^{3+} + Ag^{+}$ [37]. The third association is characteristic of inclusions of tellurium-bearing isocubanite and submarine supergene bornite enriched with U and Mo. The fourth association characterizes substitution: $(Sn^{3+} + Tl^{+}) \leftrightarrow 2Zn^{2+}$ [26]. The association of Zn with Tl could be explained by intergrowths of wurtzite with low-temperature pyrite. The fifth association reflects a combination of elevated Co, Ni, and Se in the pyrite-3.

In a fragment of the coarse-grained pyrite-wurtzite-isocubanite microfacies, the crystal habits of pyrite evolved from anhedral through euhedral and massive texture with increasing crystal sizes of the aggregates in a direction towards the conduits (Figure 4a). Most of the crystals were unzoned or had poor relic zonation. One or two zones were recognized in a single crystal (Figure 4b). Relic pseudomorphs after pyrrhotite consisted of anhedral pyrite (Figure 4c). In the conduits, this pseudomorphic pyrite was partly replaced by chalcopyrite and was surrounded by wurtzite-sphalerite aggregates (Figure 4d). Isocubanite was partly replaced by bornite mixed with sphalerite (Figure 4a,e). All of these sulfides were overgrown by later fine-grained pyrite rims (Figure 4f).

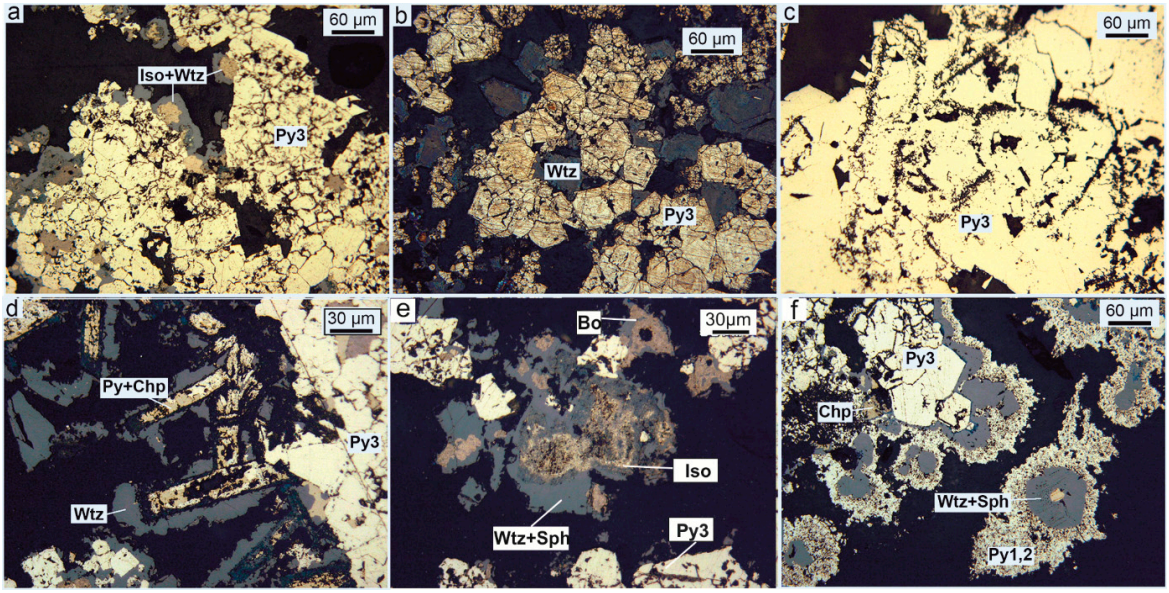

Figure 4. Pyrite-sphalerite-isocubanite microfacies (37L107d-1-2). Pobeda-2 hydrothermal field. (**a**) in granular pyrite (Py3), the walls of cavities (conduits) are overgrown by isocubanite and wurtzite (Iso+Wtz); (**b**) unzoned or poorly-zoned pyrite-3 (Py3) crystals in assemblages with wurtzite (Wtz); (**c**) relicts of pyrrhotite in coarse-grained pyrite masses (Py3); (**d**) pseudomorphs of pyrite and chalcopyrite (Py+Chp) after pyrrhotite crystals are overgrown by a rim of wurtzite (Wtz) (sample 107-11-2); (**e**) replacement of isocubanite (Iso) in the cores of wurtzite (Wtz+Sph) crystals by bornite (Bo) and minor pyrite (Py3) (in center); (**f**) sequential overgrowths of subhedral pyrite (Py3) with wurtzite (Wtz+Sph) and later fine-grained pyrite (Py1,2). Reflected light. Some pyrite varieties (b and f) are etched by HNO_3 + CaF_2.

Predominant coarse-grained anhedral and subhedral crystals of pyrite-3 were similar in trace element concentrations (Table 2, Table S2). They had high contents of Co, Ni, Se, and Bi as well as Mo, V, and U. Fine-grained pyrite had the highest concentration of Tl and Pb along with minimum mean values of Se as evidence of lower temperature of the hydrothermal fluid [19,22].

Table 2. Trace element concentration in sulfides of the pyrite-sphalerite-chalcopyrite crusts. Pobeda vent site-3. LA-ICP-MS data in ppm. Fe, Cu, and Zn is in wt.%.

Values	V	Mn	Fe	Co	Ni	Cu	Zn	As	Se	Mo	Ag	Cd	Sn	Sb	Te	Au	Tl	Pb	Bi	U
Pyrite2—anhedral porous(n = 17)																				
Mean	10	13	44.8	1012	55	1.1	0.4	205	53	86	17	4.4	1.6	8.2	0.8	0.3	5.8	60	1.4	18
Std	5.9	24	1.1	455	27	0.9	0.7	110	35	49	11	6.3	1.4	5.1	0.6	0.2	4.3	41	1.1	30
Max	24	100	46.4	1950	129	2.7	2.5	404	161	182	40	17	6	18	2.6	0.9	17	130	4	123
Med	8.6	5.3	44.7	953	46	0.8	740	190	43	69	15	0.8	1.4	8.7	0.8	0.2	6.0	47	1.0	7.2
Pyrite-3—subhedral slightly zoned to anzoned (n = 28)																				
Mean	6.2	3.6	45.5	921	50	0.8	0.1	107	52	59	11	0.8	0.8	4.2	0.6	BDL	2.2	33	1.0	17
Std	5.2	4.3	1.0	317	25	0.9	0.2	94	28	64	7.1	1.2	0.8	4.1	0.6	-	1.4	31	0.9	38
Max	19	22	46.4	1786	134	3.8	1.0	323	127	295	30	5.4	4.0	19	3	0.4	5	117	3.8	190
Med	4.7	2.3	45.8	875	46	0.6	192	72	44	40	9.0	0.4	0.5	2.3	0.4	0.1	1.9	18	0.7	3.3
Pyrite-1,2—fine-grained later masses (n = 21)																				
Mean	8.6	70	45.5	963	40	0.3	0.5	253	4.2	73	31	3.4	0.6	16	0.3	0.4	61	161	BDL	6.3
Std	2.0	52	1.2	524	27	0.3	0.9	142	3.5	58	13	5.4	0.8	7	0.2	0.6	29	142	-	12
Max	13	182	46.3	2230	102	1.4	3.9	489	12	280	66	24	3	36	0.8	3	148	475	BDL	59
Med	9.2	54	46	856	28	0.3	0.2	227	4.1	58	31	1.0	0.4	13	0.1	0.2	55	110	0.01	2.9
Isocubanite (+chalcopyrite) (n = 23)																				
Mean	0.2	8.8	38.7	1754	56	25.4	0.6	2.2	218	3.3	20	19	3.9	0.3	11.4	BDL	0.1	6.4	0.30	0.2
Std	0.2	1.8	1.9	326	92	1.9	0.4	4.2	115	5.3	11	4.9	3.1	0.9	9.1	-	0.2	21	0.39	0.4
Max	0.8	12	43.6	2576	330	27.9	2.5	20	471	23	59	27	11	4	36.8	0.3	0.9	102	1.57	1.3
Med	0.2	9.0	38.6	1730	22	25.5	4581	0.8	221	0.5	16	20	2.5	0.1	10	0.1	0.0	1.1	0.1	0.2
Würtzite (n = 38)																				
Mean	0.6	72	11.8	439	6.4	0.8	54.3	74	16	9.3	15	837	54	196	0.4	0.4	0.3	193	BDL	0.3
Std	1.3	21	3.4	283	12	0.9	3.7	70	20	23	9.3	439	81	176	0.4	0.9	0.6	198	-	0.9
Max	7.8	110	18.4	1290	47	4.4	60.0	284	96	131	33	2116	256	783	1.8	5.1	2.5	869	0.23	5.0
Med	0.1	70	11	333	0.9	0.5	55.4	60	6.9	0.4	16	752	10	147	0.2	0.1	0	141	0.01	0.05
Bornite+sphalerite mixture fine-grained (n = 11)																				
Mean	4.1	26	31.2	1944	187	15.9	18.1	165	100	180	88	133	11	37	2.8	0.5	8.8	257	0.7	67
Std	2.9	9.3	4.8	443	141	4.0	4.4	119	18	228	23	65	4	18	2.8	0.2	12	111	0.9	126
Max	9.4	48	39.6	3150	580	21.9	22.8	405	127	764	141	274	17	67	10	0.9	43	447	3.0	400
Med	3.6	27	30	1793	140	16.8	19.5	155	99	88	81	120	11	34	2.2	0.5	6	253	0.37	13
Digenite (n = 11)																				
Mean	3.4	23	6.7	2064	314	61.1	4.2	152	121	287	145	26	13	54	1.7	0.9	15	259	BDL	93
Std	1.8	3.1	6.1	399	121	7.5	3.4	35	24	132	34	20	6.3	11	1.0	0.3	6.9	84	-	91
Max	8.0	27	20.0	2750	499	71.8	9.7	214	175	530	210	66	31	70	3.3	1.4	28	408	0.7	263
Med	3.1	23	4.4	2170	310	60.5	3.8	144	116	246	135	23	12	55	1.3	0.8	12	235	0.15	45

Std, standard deviation; Max, maximum; Med, median; BDL, below detection limit.

Anhedral and subhedral varieties of pyrite-3 from Fe-Zn-Cu ores were similar to pyrite-3 from the isocubanite-pyrite microfacies in terms of most trace element contents (Figure 2, Tables 1 and 2). Pyrite-3 from pyrite-wurtzite-isocubanite microfacies had a little higher median concentration of elements due to inclusions of wurtzite (Zn, Mn, and Ag) and Cu-sulfides (Cu and Ag) and reflected a higher seawater influence (U, V, and Mo), as well.

On the series of the main diagrams, fine-grained pyrite-1 was similar to the coarse-grained variety in terms of Co, Ni, and Mo (Figure 3). In the range, fine-grained pyrite-4 had elevated contents of the low-temperature group of elements (Tl, Mn, and Pb) as compared with the high-temperature association (Te, Se, and Bi).

As well as in previous microfacies, the series of diagrams exhibited the most important positive relationships of elements: Co-Ni, Mn-Tl, Sb-As, Ag-Pb, and V-U versus a negative correlation of Se and Mo. The last two elements were related to different temperature groups (Figure 3). The results of calculation by MCW method [36] for both pyrite varieties included the follow range of mineral-chemical association: I(Cd + Zn + Au) + II(Pb + Sb + Ag) + III(Mn + Tl) − IV(As + V) + V(Mo + U) + VI(Bi + Cu) + VII(Ni + Co + Se + Te). The first association suggests a joint intergrowth of wurtzite and native gold nanoinclusions or substitution: $Au^{+} + Cd^{2+} \leftrightarrow 2Zn^{2+}$ [26]. The second association is typical for galena inclusions in terms of the well-known substitution: $2Pb^{2+} = Sb^{3+} + Ag$ (e.g., [37]). The concentration of Mn and Tl is typical of fine-grained pyrite versus euhedral pyrite (Figure 3). Seawater elements (V, Mo, U) are combined with As in the IV and V association. The positive correlation As with the

seawater group of elements suggests possible seawater influence on its concentration in the pyrite. The VI association is probably related to Cu-sulfide inclusions in pyrite. The correlation of Ni + Co + Se + Te represents high-temperature substitution of these elements into the lattice of isocubanite inclusions or directly into the euhedral pyrite.

In summary, the isocubanite-pyrite microfacies is most probably a part of the sulfide pyrite-rich crusts formed close to the feeder zone at the base of the black smoker system.

4.2. Pyrite Microfacies

Three main pyrite microfacies were recognized in Pobeda vent sites. The first pyrite-microfacies-196 was recognized in pyrite-rich crusts in diffuser fragment [35]. This crust consisted of a succession of porous fine-grained pyrite-1,2, and subhedral pyrite-2 with rare marcasite. Minor isocubanite, chalcopyrite and wurtzite-sphalerite inclusions were found at the boundary of porous and subhedral pyrite aggregates (Figure 5a). This style of pyrite crust evolution suggested replacement of initial iron sulfides by porous fine-grained pyrite and subsequent overgrowths then by crystalline pyrite-2 (Figure 5b). Greigite—Fe_3S_4 and minor pyrrhotite-$Fe_{0.8}S$ were detected as "precursors" of porous fine-grained pyrite and marcasite in the microfacies-196 (Figure 5b,c). Frequently, fine-grained pyrite varieties were partly dissolved forming atoll microtextures of pyrite-2 (Figure 5d). The pyrite-2 crystals displayed coarse oscillatory zonation recognized after etching by concentrated HNO_3 with CaF_2 powder (Figure 5e,f). The rectangular box-like pseudomorphs after pyrrhotite were sometimes preserved in coarse-zoned pyrite-2 (Figure 5f).

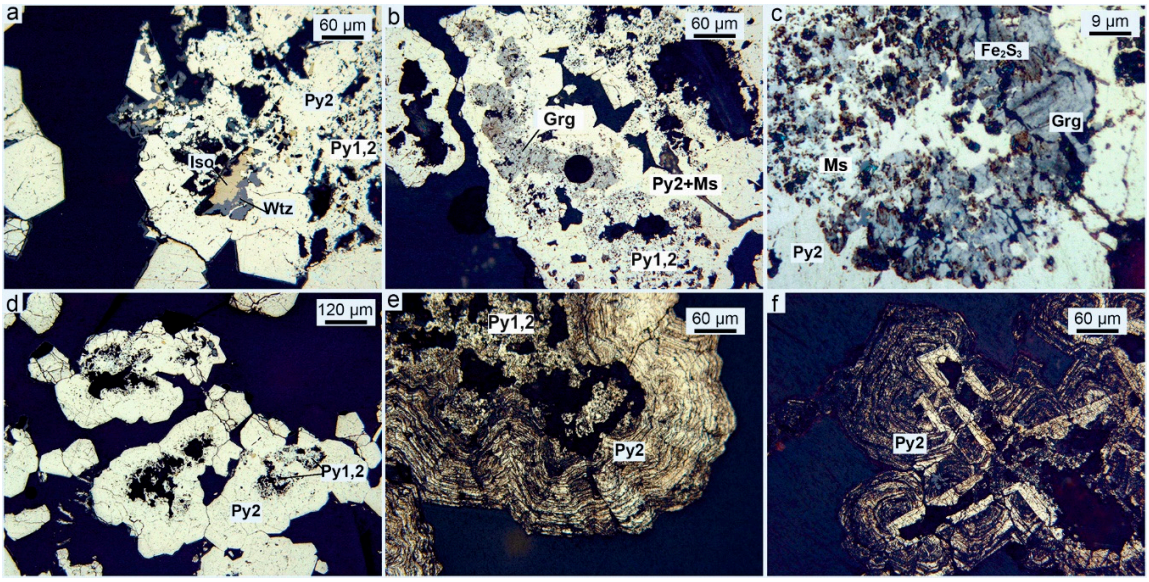

Figure 5. Varieties of pyrite in pyrite microfacies-196 (Sample 37L-196-1 and 37L-196-2). Pobeda-1 hydrothermal field. (**a**) relic inclusions of isocubanite (Iso) and wurtzite-sphalerite (Wtz) in aggregates of subhedral pyrite (Py2); (**b**) relic inclusions of greigite (Grg) with pyrrotite, marcasite (Ms), and phase Fe_2S_3 aggregates are partly replaced by porous fine-grained pyrite-1,2 (Py1,2) overgrown by subhedral pyrite-2 (Py2); (**c**) greigite (Grg) and phase Fe_2S_3 (Fe_2S_3) is replaced by pyrite-1,2 (Py2) and marcasite-1 (Ms); (**d**) atoll microtexture of pyrite-2 (Py2) with relic pyrite-1,2 (Py1,2); (**e**) oscillatory coarse-zoned pyrite-2 (Py2) envelops relic fine-grained pyrite-1,2 (Py1,2); (**f**) pyrite pseudomorphs after euhedral crystals of pyrrhotite are overgrown by oscillatory coarse-zoned pyrite-2 (Py2). Reflected light. Some pyrite varieties (e,f) are etched by HNO_3 + CaF_2.

Greigite has high concentrations of As, Mo, Ag, and Pb and low concentrations of other elements. The concentration of high-temperature elements such as Te and Bi were below detection limits (Table 3, Table S3). In the pyrite-1,2 and pyrite-2, the mean concentration of most trace elements (except U) and

the Co/Ni ratios >1 were likely inherited from the greigite (Table 3). Se, Mn, and U, as well as the Co and Ni contents are higher in pyrite-2, especially in the assemblages isocubanite and wurtzite (Table 3, Table S3).

Table 3. Trace element contents in sulfides of third style pyrite crusts. Pobeda vent site. LA-ICP-MS data in ppm. Fe Cu. Zn are in wt. %. (sample-196).

Values	V	Mn	Fe	Co	Ni	Cu	Zn	As	Se	Mo	Ag	Cd	Sn	Sb	Te	Au	Tl	Pb	Bi	U
1. Greigite—Fe_3S_4 (1)																				
content	4.1	85	56.6	19.7	6.9	0.16	0.09	1284	1.8	128	25	5.3	3.8	1.8	0.21	0.7	1.1	119	BDL	1.2
2.Pyrite-1 fine-grained (44)																				
Mean	5.5	100	46.2	12	2.9	0.14	0.13	320	4.1	91	8.8	3.5	2.7	1.3	0.2	0.5	3.0	64	BDL	5.8
Std	3.9	160	0.2	13	3.2	0.07	0.23	440	3.8	42	6.0	5.0	2.2	0.8	0.2	0.7	2.0	40	–	8.1
Max	16	866	46.5	52	19	0.34	1.35	2398	17	181	23	29	13	3.8	1.1	3.7	7.7	153	1.8	38
Med	4.6	36	46.2	6.0	2.0	0.13	0.05	185	3.6	86	7.0	1.7	2.1	1.2	0.1	0.3	2.4	54	0.01	3.0
3.Pyrite-2 coarse banding oscillatory-zoned (30)																				
Mean	3.2	177	46.4	2.5	1.0	0.01	0.02	176	1.7	68	0.4	0.4	0.4	0.6	0.2	0.1	7.6	17	BDL	1.2
Std	1.0	141	0.0	2.6	0.7	0.01	0.02	136	2.0	28	0.6	0.5	0.4	0.3	0.1	0.1	5.2	22	–	1.1
Max	5.5	449	46.5	10	2.9	0.04	0.12	820	7.9	110	2.2	1.6	2.0	1.4	0.4	0.7	30	72	BDL	3.8
Med	2.9	133	46.4	1.5	0.7	0.01	0.01	172	1.0	71	0.2	0.2	0.3	0.5	0.1	0.04	6.0	9.0	0.00	0.8
4.Pyrite-2 coarse banding oscillatory-zoned with inclusions of isocubanite and würtzite (21)																				
Mean	6.0	44	46.0	40	10	0.09	0.34	212	6.4	112	5.1	5.1	7.3	1.3	0.2	0.2	5.2	36	BDL	15
Std	8.4	26	0.4	77	19	0.04	0.43	136	7.2	46	3.0	5.5	15	0.6	0.1	0.1	2.7	21	-	27
Max	42	93	46.4	317	79	0.17	1.49	580	31	183	11	18	68	2.5	0.7	0.5	11	69	0.9	96
Med	4.2	38	46.2	8.3	2.0	0.08	0.13	185	3.9	116	5.8	2.6	2.0	1.1	0.1	0.2	4.0	39	0.01	5.1

Std, standard deviation; Max, maximum; Med, median; BDL, below detection limit.

Normalization of pyrite-1,2 of the pyrite-rich microfacies-196 to pyrite-1,2 of the pyrite-wurtzite-isocubanite microfacies displayed the following series of ratios: Sn (5) → Cd (1.7) → Au (1.6) → Mo (1.5) → Bi (1.2) → Se (0.9) → As (0.8) → Te (0.8) → Mn (0.7) → Pb (0.5) → Cu (0.5) → Ag (0.2) → Sb → (0.1) → Ni (0.1) → Tl → (0.04) → Co (0.01). Pyrite-1 of the pyrite microfacies contained a little more Sn, whereas contents of Ag, Sb, Ni, Tl, and Co were much higher of the pyrite-1,2 in pyrite-wurtzite-isocubanite microfacies.

Pyrite-2 of microfacies-196 normalized to pyrite-3 of the wurtzite-isocubanite microfacies exhibited the following ratios: Mn (37) → Ni → (1.9) → Te (1.0) → Se (0.9) → Sn → (0.7) Au (0.6) → Cd (0.5) → Bi (0.41) → Tl (0.39) → Ag (0.15) → Mo (0.14) → Zn (0.14) → Pb (0.13) → Cu (0.10) → V (0.05) Co (0.04) → Sb (0.03) → U (0.02) → As (0.01). Mn was the predominant element in coarse-zoned pyrite-2, whereas poorly zoned pyrite-3 was enriched in a wide group of elements related to microinclusions Cu-sulfides, galena (Pb, Sb, and Ag), cobaltite, and wurtzite. The concentration of seawater elements (Mo, U, and V) was also higher in pyrite-3.

The calculation by the MCW method [36] using all these types of pyrite (sample 37L-196) yielded the following mineral-chemical associations: I(Co + Ni + Se + Bi + Te) + II(Sn + Zn + Cd) + III(Sb + Au + As) + IV(Pb + Ag + Cu) + V(Mo + V + U) − Tl − Mn. The first association includes high-temperature trace elements related to pyrite-2 found in the assemblages with isocubanite and wurtzite. The second association is interpreted to reflect the presence of wurtzite inclusions that are enriched in Sn. The third and fourth associations may indicate an assemblage of invisible tennantite and native gold nanoinclusions in pyrite. The fifth association includes the seawater-derived elements (e.g., [12]).

On the several diagrams (Figure 5), all pyrite varieties of microfacies-196 formed compact clusters of points independent of crystal habits and sizes. The greigite and fine-grained pyrite had similar trace element compositions (Table 3, Figure 6). In the Co-Ni diagram, the area of trace element distribution related to pyrite of microfacies-196 is considered as an elongation of the isocubanite-pyrite and pyrite-isocubanite-wurtzite range (Figure 6a).

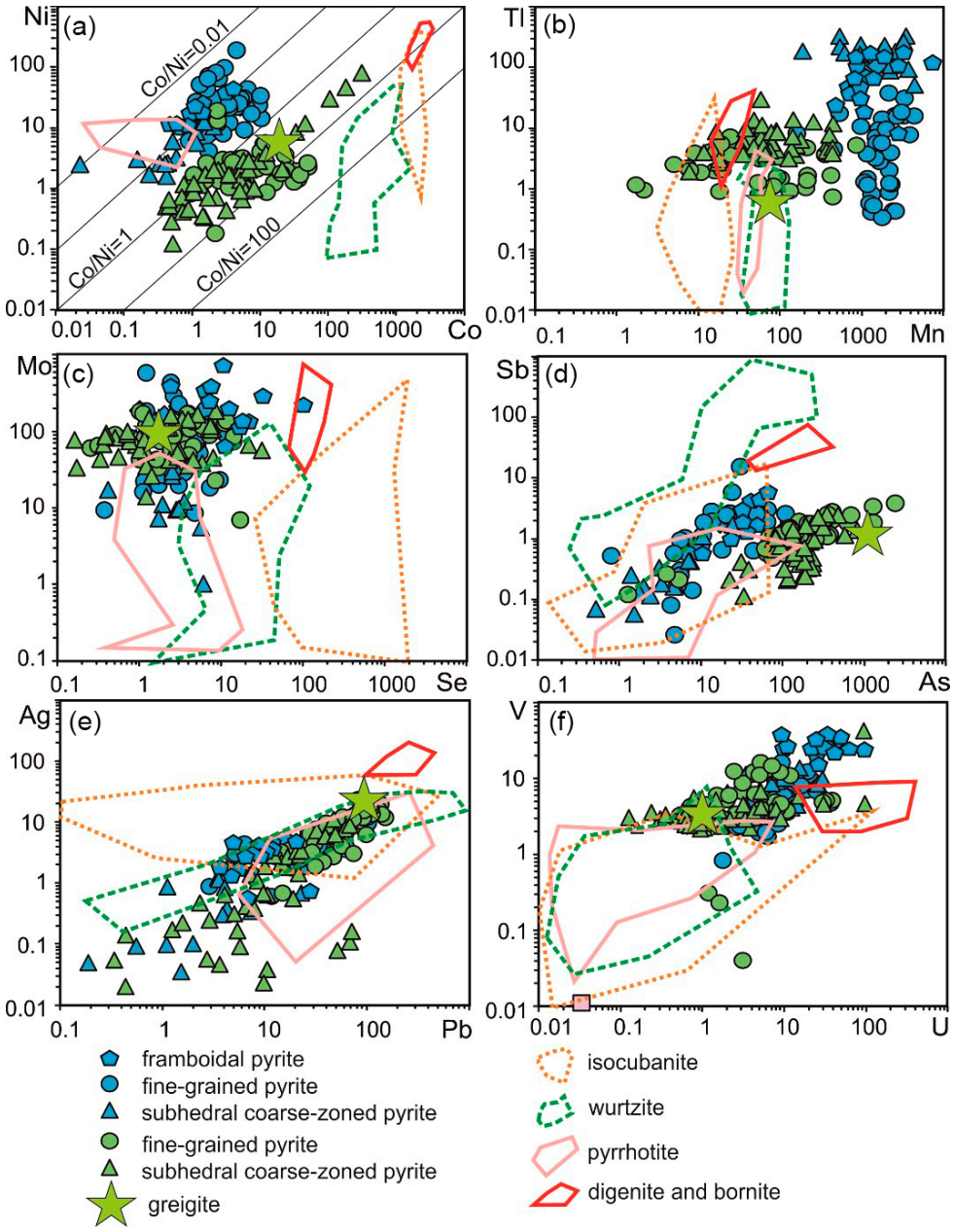

Figure 6. Diagrams of trace elements in sulfides of pyrite microfacies-196 and -195. Pobeda-1 hydrothermal field. (**a**) Co vs Ni ratio; (**b**) Mn vs Tl ratio; (**c**) Se vs Mo ratio; (**d**) As vs Sb ratio; (**e**) Pb vs Ag ratio; (**f**) U vs V ratio.

Friable aggregates of pyrrhotite with minor sphalerite, talc, and calcite occurred in ore body-1 at Pobeda-1 hydrothermal fields [35] (Figure 7a). The fragmental pyrite microfacies-I95 is a little different from the pyrite-rich microfacies-196 with respect to lack of visible inclusions of wurtzite and isocubanite. Relicts of pyrrhotite instead of greigite was retained in fine-grained pyrite of microfacies-195 (Figure 7b). Boxy fine-grained pyrite pseudomorphs after pyrrhotite crystals with typical relic cleavage were recognized in the pyrite microfacies-195 (Figure 7c,d). Another specific feature was the abundance of framboidal pyrite in the cores of coarse oscillatory-zoned pyrite aggregates (Figure 7e). Rare relic colloform pyrite was found in the core of coarse-zoned pyrite-2 clusters (Figure 7f).

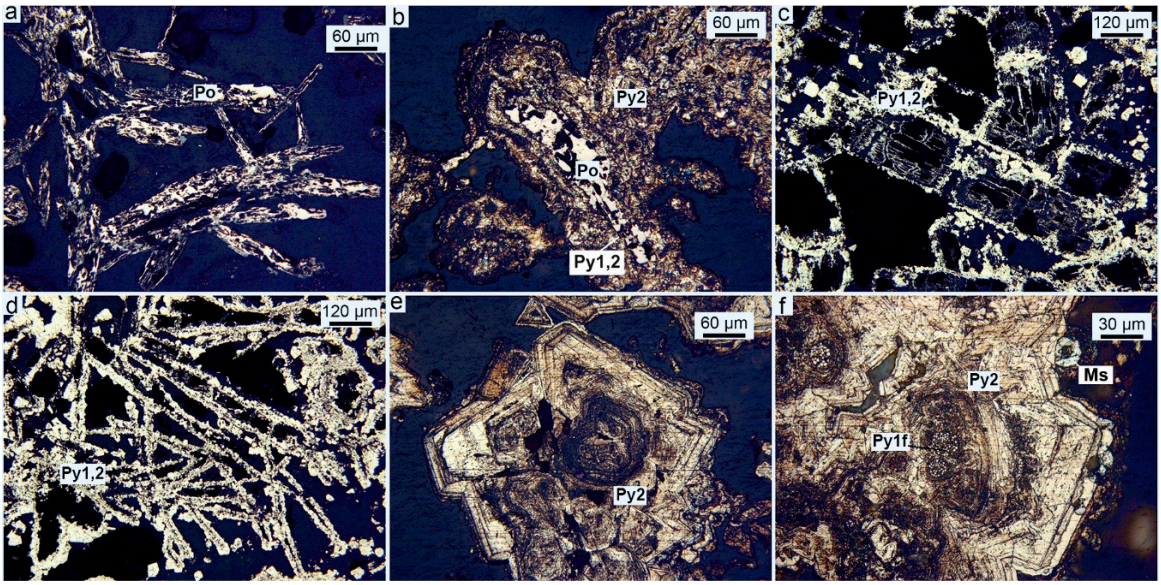

Figure 7. Varieties of pyrite in pyrite microfacies-195. Pobeda-1 hydrothermal field. (**a**) subhedral elongate pyrrhotite (Po) crystal framework; (**b**) relic inclusion of pyrrhotite (Po) is overgrown by subhedral pyrite-2 (Py2) (37L-195-2); (**c**) box-like pseudomorphs of pyrite (Py1,2) after pyrrhotite crystals (**d**) network microtexture of pyrite aggregates (Py1,2) formed after friable pyrrhotite masses; (**e**) oscillatory coarse-zoned pyrite-2s (Py2) envelops relic colloform pyrite (37L-195-2); (**f**) relict inclusions of framboidal pyrite (Py1f) in coarse-zoned pyrite-2 (Py2) (37L195-3). Reflected light. Some pyrite varieties (b,e,f) were etched by HNO_3 + CaF_2.

Pyrrhotite had low amounts of trace elements in the studied samples (Table 4, Table S4). The values of Co/Ni ratio were very low (0.01–0.08).

Table 4. Trace element concentration in pyrrhotite and varieties of pyrite of microfacies-195. Pobeda vent site. LA-ICP-MS data in ppm. Fe, Cu, and Zn are in wt.% (samples 37L-195-1, 37L-195-2, and 37L-195-3).

Values	V	Mn	Fe	Co	Ni	Cu	Zn	As	Se	Mo	Ag	Cd	Sn	Sb	Te	Au	Tl	Pb	Bi	U
1. Pyrrhotite-Po (32)																				
Mean	1.1	46	63	0.3	7.5	0.11	0.06	12	3.2	8.0	5.7	0.7	3.3	0.2	1.0	0.2	0.7	80	0.3	0.7
Std	0.8	11	0.9	0.2	2.4	0.07	0.12	28	3.0	13	5.7	1.8	2.4	0.3	1.7	0.1	1.0	98	0.2	1.5
Max	2.8	78	64	0.9	13	0.33	0.70	164	15	51	30	10	12	1.3	8.0	0.6	4.3	453	0.7	6.9
Med	1.0	42	63	0.2	6.9	0.1	0.03	5.0	2.2	3.1	4.4	0.1	2.9	0.0	0.2	0.2	0.3	43	0.2	0.1
2. Framboidal pyrite—Py1f (23)																				
Mean	26	1597	45.8	2.1	19.4	0.4	0.1	37	BDL	207	2.7	BDL	6.7	2.4	BDL	1.3	85	11	0.2	32
Std	6.4	1454	0.4	1.3	7.9	0.4	0.03	14	-	144	1.5	-	3.3	1.1	–	0.5	46	8.1	0.1	18
Max	40	7460	46.2	5.2	41	1.7	0.2	66	BDL	726	7.7	BDL	19	5.6	BDL	2.2	164	34	0.5	94
Med	25	1073	46	1.6	19	0.3	0.06	36	8.0	160	2.8	0.9	6.4	2.3	3.1	1.3	91	7.7	0.1	28
3. Fine-grained pyrite-1,2ap in boxy pseudomorphs after pyrrhotite—Py1,2 (36)																				
Mean	5.3	1912	46.1	4.0	36	0.2	0.04	26	4.0	107	4.9	0.2	2.4	2.0	0.5	0.3	7.8	39	0.11	11
Std	3.2	930	0.2	2.6	34	0.1	0.04	29	2.7	120	2.8	0.2	1.4	2.6	0.4	0.4	9.0	22	0.08	7.1
Max	16	4420	46.3	11	187	0.5	0.16	121	14	580	13	1.2	7.3	15	1.8	2.1	38	104	0.34	37
Med	4.9	1775	46.1	3.5	24	0.1	0.02	14	3.1	71	4.2	0.1	2.2	1.9	0.3	0.2	4.3	34	0.1	8.9
4. Pyrite coarse banding oscillatory-zoned—Py2 (15)																				
Mean	8.4	1972	46.2	0.9	6.0	0.12	0.02	6.3	3.1	30	0.8	0.6	2.6	0.5	0.2	0.9	191	9.3	BDL	11
Std	3.2	1338	0.2	0.7	4.7	0.14	0.01	7.1	1.4	27	1.1	0.8	2.6	0.5	0.2	0.4	83	15	-	8.7
Max	14	4450	46.5	2.1	16	0.57	0.05	25	6.0	84	4.1	3.0	11	1.7	0.7	1.9	333	52	0.1	29
Med	6.9	1740	46	0.5	3	0.1	0.01	3.3	2.5	17	0.4	0.1	1.8	0.2	0.2	0.7	166	3.6	0.04	7.4

Std, standard deviation; Max, maximum; Med, median; BDL, below detection limit.

Framboidal pyrite–Py1f of microfacies-195 is characterized by high concentrations of low-temperature (Mn, Tl) and seawater-derived (Mo, U, and V) elements in comparison to coarse-crystalline pyrite. In framboidal pyrite, the average Au concentration (1.5 ppm) exceeded the average contents calculated for pyrrhotite and other pyrite varieties. On the other hand,

the concentration of the elements of the high-temperature association (Se, Co, Te, and Bi) and moderate temperature association (As and Sb) were relatively low in framboidal pyrite in comparison with pyrite-3 of isocubanite-rich microfacies (Table 1, Table 2, and Table 4). There were no significant differences in trace element concentrations in framboidal and fine-grained pyrite. The Co/Ni ratios < 1 were typical for framboidal pyrite as well as for pyrrhotite.

The porous fine-grained pyrite-1,2 formed after pyrrhotite was similar in trace element contents to the same pyrite variety in pyrite facies-196. The pyrite-1,2 variety was enriched in Mn and Mo in comparison to the contents in the pyrrhotite (Table 4, Table S4). In this pyrite-1 of microfacies-195, the Co/Ni ratios were commonly less than 1, whereas in pyrite of abovementioned microfacies-196, the Co/Ni ratios were much higher than 1.

Coarse banding oscillatory-zoned pyrite-2 of microfacies-195 inherited most values of trace element contents from framboidal and fine-grained pyrite. The exception was higher contents of Tl in the coarse-zoned pyrite (Table 1, Table 2, and Table 4). The pyrite-2 was different from pyrite-3 of isocubanite-pyrite and pyrite-wurtzite-isocubanite microfacies by low concentrations of high-temperature elements such as Co, Ni, Se, Te, and Bi versus low-temperature (Mn and Tl) and seawater (U, V, and Mo) elements. The abundance of Mn, Tl, Ni, and U and Co/Ni < 1 were typical features of all pyrite varieties related to microfacies-195 (Figure 5).

The range of poorly recognized mineral-chemical associations related to pyrite of microfacies-195 was calculated by the MCW method: I(Pb + Ag + Co) + II(Bi + Se + Te) + Cd + III(V + Au + Tl) − IV(Sn + U + Cu) + V(Zn + As + Ni) − Mo − Sb − Mn. The first association reflects the composition of a fine-grained pyrite, which is slightly enriched in Pb, Ag, and Co. The second association (Se, Bi, and Te) commonly classified as a high-temperature assemblage (i.e., Hannington et al., 1999 and Discussion herein) has very low contents of the elements. The third association is typical of framboidal pyrite inclusions. The fourth and fifth associations are probably related to supergene Cu-sulfides mixed with sphalerite.

4.3. Marcasite-Pyrite Microfacies

The marcasite-pyrite microfacies-107-10 displayed diverse microtextures. The compact framework of marcasite-pyrite crust contained a lot of cavities. The cavities were filled with porous pyrite masses made of relic spongy pyrite-1 that were pseudomorphic after pyrrhotite crystals. The elongate pores were inherited from the relic cleavage typical of pyrrhotite crystals (Figure 8a). Microinclusions of iron monosulfide are found in spongy pyrite. The pyrite-1 pseudomorphs were overgrown by later coarse-crystalline aggregates of pyrite-2 subhedral crystals (Figure 8b). In other cases, the pyrite formed box-like pseudomorphs. The net-like microtextures were common for box-like pseudomorphic pyrite aggregates (Figure 8c). Uraninite-UO_2 inclusions were disseminated in subhedral pyrite-2. Successive overgrowths of spongy pyrite-1 by subhedral marcasite and pyrite were observed (Figure 8d). Locally, marcasite-pyrite masses were brecciated (Figure 8e). Reniform microtextures occurred in marcasite-pyrite crystalline masses (Figure 8f). Colloform, radiated, and oscillatory-zoned marcasite were common (Figure 8g–i). The sooty colloform marcasite became black during second etching by HNO_3 + CaF_2. Framboidal pyrite was rare in this microfacies.

Some means and maximums of trace element contents (Co, Ni, Se, As, Ag, Pb, Bi Mo, Tl, and U) and Co/Ni ratios were much higher (1.4–2.2) in the spongy pyrite than in pyrrhotite (Tables 4 and 5). Poorly zoned crystalline pyrite-2 that surrounded the pseudomorphic spongy pyrites was depleted in Ag and Au but was enriched in seawater elements (Mo and U) in comparison to spongy pyrite and pyrrhotite (Tables 4 and 5, Tables S4 and S5). In comparison with pyrite-3 of pyrite-wurtzite-isocubanite microfacies, this pyrite-2 was depleted in Co, Zn, Cu, and Ag, but not in Mn.

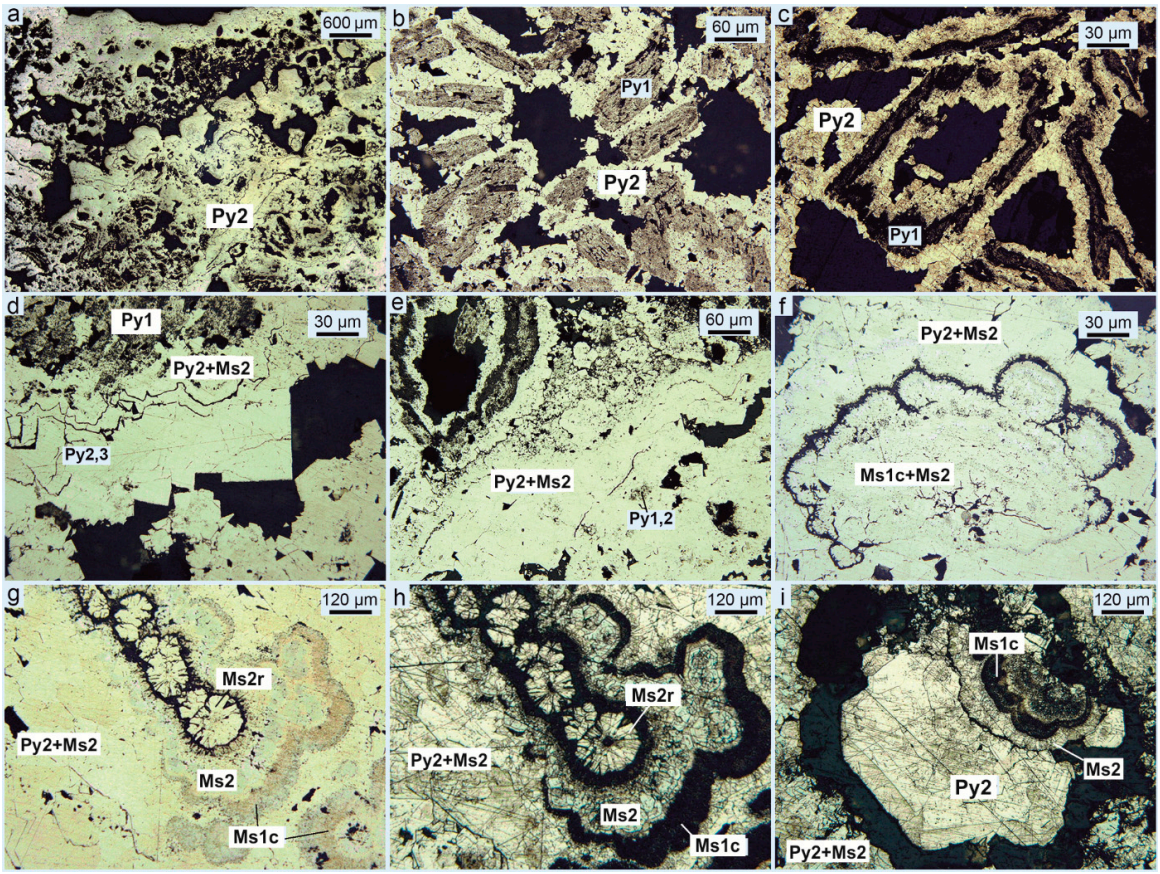

Figure 8. Varieties of pyrite in reniform-rich pyrite microfacies of the hydrothermal crusts (sample 37L-107-10). Pobeda-2 hydrothermal field. (**a**) porous marcasite-pyrite (Py2) crust; (**b**) pseudomorphic spongy pyrite-1 (Py1) is overgrown by anhedral and subhedral crystals of pyrite (Py2); (**c**) pyrite-2 (Py2) aggregates envelop and drape over boxy spongy pyrite pseudomorphs (Py1) after pyrrhotite; (**d**) successive overgrowth of pyrite-1 (Py1) by subhedral marcasite (Py2+Ms2) and pyrite (Py2,3); (**e**) brecciated marcasite-pyrite (Py2+Ms2) aggregates; (**f**) reniform marcasite-1 and -2 (Ms1c+Ms2) in crystalline marcasite-pyrite (Py2+Ms2) aggregates; (**g**,**h**,**i**) overgrowth of colloform (Ms1c) and radiated (Ms2r) marcasite by crystalline marcasite (Ms2) and marcasite-pyrite (Py2+Ms2) aggregates. Reflected light. Some pyrite varieties (c,h,i) are etched by HNO_3 + CaF_2.

Colloform-like marcasite-1 had marginally higher concentrations of Mn and Ag in comparison with crystalline pyrite varieties. In general, all marcasite varieties of the hydrothermal crusts had low concentrations of the most studied trace elements except for Mo and Mn. The Mn concentration decreased from colloform to radial and subhedral marcasite varieties. In all these iron sulfides, the Co/Ni ratios were <1. Spongy pyrite-1sp had much higher contents of most trace elements, except Mn, than marcasite-1c (Table 5, Table S5). The data are illustrated in Figure 9. Despite lower concentrations of Co and Ni (Figure 9a), marcasite showed the same linear distribution for these elements as the pyrite of microfacies-195 (Figure 9b–f). The Mo contents were much higher in marcasite than in pyrrhotite (Figure 9c). Marcasite plotted points showed lower concentrations of As, Ag, and U in comparison to pyrite in the following diagrams (Figure 9d-f). Uraninite was found in subhedral pyrite-2,3 only.

Table 5. Trace element contents in pyrite varieties of marcasite-pyrite microfacies. Pobeda-2 hydrothermal field. LA-ICP-MS data in ppm, Fe, Cu, and Zn in wt.%.

Values	V	Mn	Fe	Co	Ni	Cu	Zn	As	Se	Mo	Ag	Cd	Sn	Sb	Te	Au	Tl	Pb	Bi	U
1. Spongy pseudomorphic pyrite-1 after suhedral pyrrhotite (20)																				
Mean	3.5	4.9	46.3	178	96	0.11	0.01	259	52	69	31	0.7	2.7	2.0	1.0	0.5	9.0	169	2.4	4.5
Std	0.7	9.0	0.03	21	15	0.03	0.01	74	18	35	22	0.3	1.9	0.9	0.4	0.1	2.7	34	0.9	3.4
Max	4.7	42	46.4	219	125	0.23	0.04	455	96	173	93	1.6	10	4.9	1.8	0.9	14	226	4.5	11
Med	3.7	2.4	46.3	175	94	0.10	0.01	262	47	57	26	0.6	2.1	1.8	1.0	0.5	8.3	172	2.2	3.5
2. Pyrite-2 anhedral to subhedral poor-zoned (20)																				
Mean	2.5	75	46.4	34	17	0.08	0.01	91	20	134	1.9	0.2	0.5	0.7	0.9	0.1	6.4	20	3.8	28
Std	2.1	108	0.2	44	26	0.16	0.01	65	19	340	1.9	0.2	0.5	0.6	3.0	0.1	7.1	16	12	87
Max	9.1	429	46.5	173	104	0.72	0.03	231	73	1570	6.8	0.8	2.3	2.4	14	0.4	22	57	55	390
Med	2.0	35	46.5	18	10	0.02	0.00	70	15	49	1.1	0.1	0.2	0.6	0.2	0.04	3.3	15.1	0.6	3.7
3. Colloform-like macasite-1 (18)																				
Mean	2.1	1511	46.3	1.5	2.1	0.02	0.01	30	5.1	76	12	0.3	4.2	0.5	0.8	0.1	4.0	9	BDL	0.9
Std	1.9	1030	0.1	2.0	2.2	0.02	0.01	32	2.3	47	15	0.2	8.9	0.4	0.7	0.1	3.9	15	-	1.1
Max	8.6	4120	46.4	7.0	8.3	0.10	0.06	137	10	219	48	0.8	38	1.1	2.2	0.3	15	61	1.2	3.7
Med	1.5	1470	46.3	0.4	1.3	0.01	0.01	15	5.5	70	3.7	0.3	0.6	0.2	0.8	0.1	2.5	2.5	0.1	0.3
4. Radial marcasite—Ms2r (30)																				
Mean	1.5	793	46.4	1.1	1.6	0.00	0.02	16	5.8	81	2.5	0.4	0.5	0.8	1.1	0.05	2.5	1.4	BDL	0.5
Std	0.7	608	0.1	1.9	2.1	0.01	0.07	7.3	3.3	30	3.8	0.3	0.6	0.5	1.2	0.03	1.9	1.2	-	0.7
Max	3.4	2730	46.5	9.3	9.7	0.03	0.33	40	16	168	16	1.9	2.8	2.1	4.1	0.16	7.5	4.6	0.23	3.3
Med	1.4	560	46.4	0.5	0.9	0.00	0.01	15	5.5	72	0.9	0.2	0.3	0.6	0.7	0.05	2.3	1.3	0.1	0.2
5. Marcasite anhedral to subhedral–Ms2 (21)																				
Mean	0.9	401	46.5	0.1	0.4	0.00	0.00	19	5.2	94	0.7	0.5	0.2	B	2.1	0.07	3.6	1.1	BDL	0.2
Std	0.3	186	0.0	0.1	0.3	0.00	0.00	7.5	2.5	44	0.6	0.3	0.3	0.1	1.3	0.05	5.4	1.8	-	0.2
Max	1.6	743	46.5	0.4	1.3	0.00	0.01	45	11	229	2.1	1.4	1.3	0.3	4.7	0.23	26	8.7	0.10	1.0
Med	0.9	370	46.5	0.1	0.5	0.00	0.00	18	5.5	83	0.4	0.3	0.2	0.1	1.7	0.1	1.7	0.6	0.0	0.1

Std, standard deviation; Max, maximum; Med, median; BDL, below detection limit.

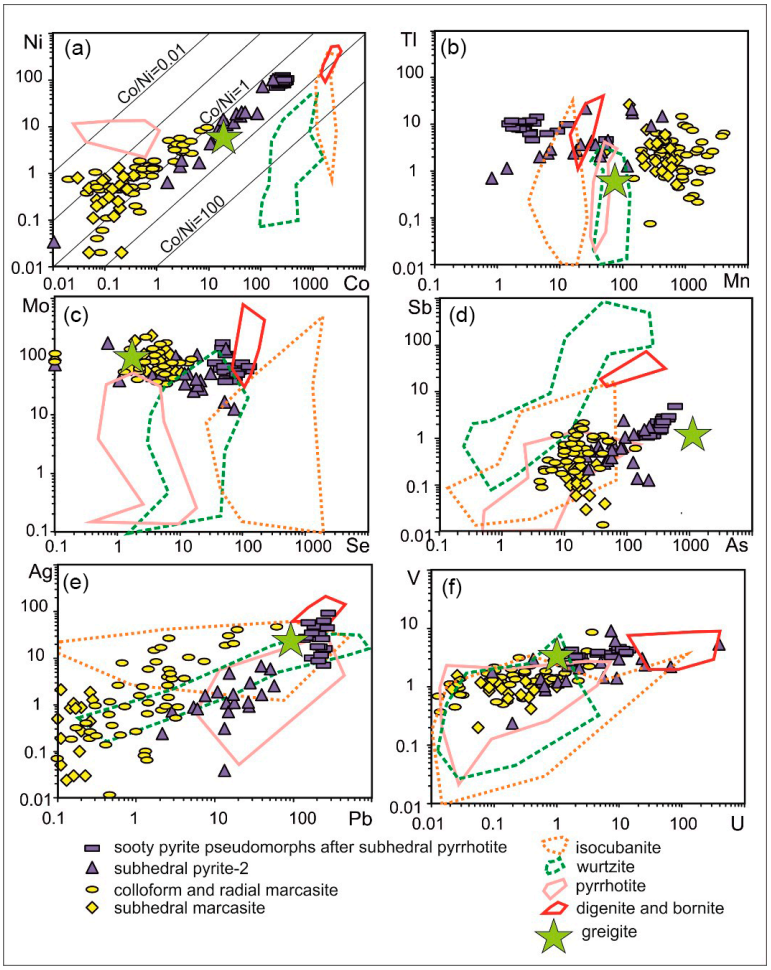

Figure 9. Diagrams of trace elements concentrations in sulfides of marcasite-pyrite crust (sample 37L-107-10). Pobeda-2 hydrothermal field. (**a**) Co vs Ni ratio; (**b**) Mn vs Tl ratio; (**c**) Se vs Mo ratio; (**d**) As vs Sb ratio; (**e**) Pb vs Ag ratio; (**f**) U vs V ratio.

In general, pyrite varieties in the marcasite-pyrite microfacies were characterized by the following mineral-chemical associations calculated using the method of maximum correlation range: I(Co + Ni) + II(Pb + Au + As + Sb + Ag+Se) + III(Cd + Zn) + IV(Cu + U + Mn) − Tl − Mo − V − Sn − V(Te + Bi). The first and second associations pertain to spongy pyrite. The association-III corresponds to wurtzite or sphalerite invisible inclusions. In Cu- and Mn-bearing pyrite-2, microinclusions of uraninite yield association-IV. The fifth association and maximum contents of Te (12 ppm) and Bi (55 ppm) may be inferred to indicate the presence of Bi-telluride nanoinclusions in pyrite-2.

In general, marcasite varieties were characteristic of the following mineral chemical associations: I(Pb + Sn + Cu + Bi + Ag) + II(As + V + U) + III(Co + Ni + Zn) + IV(Te + Se) − Sb − Tl − Au − Cd − V(Mo + Mn). The first association is typical of galena and chalcopyrite microinclusions. The second association indicates a correlation of As with seawater elements. The third association may suggest that the Co and Ni contents are a little higher in radial marcasite-1 containing Zn (wurtzite or sphalerite microinclusions. Positive correlation of Se with Te indicates that both of these elements substitute for S in the marcasite. The fifth association may reflect coeval concentration of Mn and Mo in marcasite. Nevertheless, we have to stress that this interpretation was less than robust because the presence of nanoinclusions cannot be excluded and the concentrations of most trace elements in marcasite was too low.

5. Discussion

5.1. The Mineral Evolution in the Suite of Pyrite-Bearing Microfacies

The massive sulfides of the Pobeda hydrothermal SMS deposit are subdivided into five main mineral microfacies: (1) isocubanite-pyrite, (2) pyrite-wurtzite-isocubanite, (3) pyrite with subordinate isocubanite and wurtzite-sphalerite microinclusions, (4) pyrite-rich with framboidal pyrite, and (5) marcasite-pyrite. Spongy, framboidal, and fine-grained pyrite and rare marcasite varieties replaced pyrrhotite, greigite, and mackinawite "precursors." Pyrrhotite replacement by pyrite occurs over a broad range of temperatures [13]. The later coarse and fine banding oscillatory-zoned pyrite and marcasite crystals are overgrown and/or replaced by unzoned subhedral and euhedral pyrite-3.

In the general compiled microfacies suite, the amounts of isocubanite, wurtzite, and unzoned euhedral pyrite decrease while the concentrations of framboidal, fine-grained, and spongy pyrite and also marcasite and its colloform and radial varieties increase. This progression reflects evolution from black and gray (grayish white) smoker to clear smoker or diffuser microfacies. In the same range of microfacies, temperature declined and pH increased due to mixing of hydrothermal fluids with cold seawater (e.g., [13]). The seawater mixing model predicts remobilization of Zn at intermediate temperatures (275–325 °C) and low pH during formation of isocubanite-pyrite microfacies and reprecipitation of ZnS at lower temperature and higher pH. (e.g., [13]). Diffuse fluids that formed pyrite-rich microfacies have less Zn as the temperature decreases with increased mixing with seawater. Framboidal pyrite is commonly considered as diagenetic or sedimentary pyrite varieties formed as a product of initial sooty iron sulfide, e.g., mackinawite. The reactions of FeS, either as pyrrhotite or mackinawite, with H_2S to form pyrite were confirmed (e.g., [38]).

In the marcasite-pyrite sample, two microfacies are combined in the hydrothermal crusts of diffuser fragments. The inner part located close to the conduit is a composite of sooty and spongy pyrite pseudomorphs after subhedral pyrrhotite, overgrown by anhedral and subhedral pyrite. The outer part of the crust consists of reniform sooty and radial marcasite, and also framboidal pyrite, followed by crystalline anhedral and subhedral marcasite and pyrite varieties. Marcasite forms under low-temperature (<240 °C) acidic or H_2S-deficient conditions, whereas pyrite forms in relatively higher pH or H_2S-rich conditions [39,40].

In general, this progression could be interpreted as a proxy for temperature and H_2S concentration decline due to mixing of hydrothermal fluids with seawater in a diffusive hydrothermal system.

Secondary bornite, digenite, covellite, geerite, and goethite replaced isocubanite, chalcopyrite, and chalcopyrite-rich wurtzite during coeval and later submarine supergene processes.

5.2. Trace Element Concentration, Forms, and Associations in Pyrite Varieties

A trace element temperature classification has been used by many geologists who studied geochemical features of sulfides in modern SMS [12,14,16,18,26,28,41,42] and ancient VMS (volcanogenic massive sulfide) [4,43,44] deposits. Besides the temperature of precipitating fluid, the enrichment of trace element could be related to type of host rocks (high Ni contents in sulfides is often considered to be an indicator of ultramafic substrates). In our case study, trace elements are subdivided into four associations: (1) high temperature—Cu, Se, Te, Bi, Co, and Ni; (2) mid temperature—Zn, As, Sb, and Sn; (3) low temperature—Pb, Sb, Ag, Bi, Au, Tl, and Mn; and (4) seawater—U, V, Mo, and Ni. This classification can be applied to Pobeda microfacies, only, because each hydrothermal field has its own geochemical specialization. The main problem for a correct interpretation of element associations is the difficult discrimination between elements forming discrete mineral phases (microinclusions) and those concentrated in the host lattice structure. For instance, elevated Ni contents in high-temperature microfacies at Pobeda hydrothermal field are related to influence of ultramafic rocks. Despite the obvious role of substrate rocks as metal sources, their composition (specifically mafic vs. ultramafic) does not emerge as a statistically significant independent factor. A large part of the observed variability is produced by a combination of three independent factors, which are interpreted to reflect (in order of importance): (1) the temperature of deposition, (2) the ridge spreading rate, and (3) zone refining [45]. On the other hand, e.g., predominance of Ni above Co could be signature of diagenetic process in low-temperature pyrite microfacies.

***Cu, Se, Te, and Bi*:** This group of elements is mostly concentrated in isocubanite and chalcopyrite. Less variable Se and Te contents are detected in sphalerite and wurtzite (Table 2). The most important host for isocubanite-chalcopyrite inclusions is subhedral and euhedral pyrite-3 of isocubanite-pyrite and pyrite-wurtzite-isocubanite microfacies at the Pobeda vent site. The contents of Cu and Se in all pyrite varieties decrease in the series from isocubanite-pyrite to pyrite and marcasite-pyrite microfacies (Figure 10). The highest contents of Cu and Se are detected in pyrite-3 and in spongy pyrite-1 from conduits (Figure 10a,c). The Se contents are correlated with Te because Se^{2-} provides expansion of the lattice which is favorable for Te^{2-} substitution in sulfides [41]. Isocubanite-chalcopyrite, pyrite-3, and framboidal pyrite are the hosts for high Te (Figure 10f). In other pyrite varieties, Te and Bi contents are dramatically low or even below detection limits (Figure 10d,f).

The high-temperature assemblages which consist of chalcopyrite and pyrite are expected to have elevated Se and Te concentrations, since Te and Se substitute for S at high temperatures [46]. The general enrichment in Se depends on the fluid temperature, e.g., the high solubility of Se in fluids occurs at temperatures of >350 °C [12,18,28,41,44,47,48]. In contrast, Se-poor chalcopyrite has been found to precipitate at medium to low temperatures [49]. Low concentrations of Te in sulfides could be explained by lack of a magmatic contribution [50,51] or phase separation [18] in the hydrothermal system of Pobeda vent sites.

In mafic and ultramafic sequences, the fluids do not deviate significantly from the pyrite–pyrrhotite redox buffer, even after significant mixing with seawater and cooling, because of high concentrations of reduced components such as H_2, H_2S, CH_4, and ferrous iron (e.g., [52]). The modern and ancient smokers expel Te^{2-} in the pyrrhotite-rich plume likely due to high temperatures, coupled with reducing conditions, leading to Te undersaturation of the hydrothermal fluid. Low contents of Te could be also a proxy of a relatively immature hydrothermal system as calculated in a model of seawater interaction with ultramafites and basalts at 300 °C [53].

The interquartile ranges (IQR) could be considered as indicators of the pyrite and marcasite crystallization conditions. It is inferred that the combination of elevated concentration of trace elements related to high-temperature association with narrow interval of IQR indicates the fast precipitation of

the sulfides from hydrothermal fluids in contrast to slowly grown oscillatory-zoned pyrite formed by hydrothermal as well as diagenetic coeval processes (Figure 10).

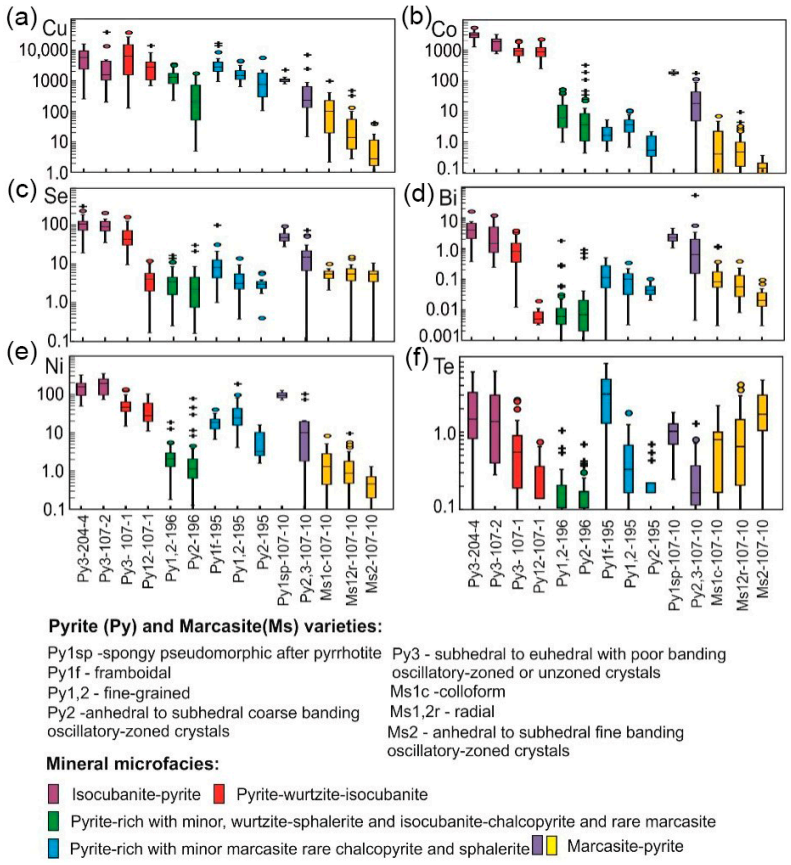

Figure 10. Whisker-and-box plots for the high-temperature association of elements Cu (**a**), Co (**b**), Se (**c**), Bi (**d**), Ni (**e**), and Te (**f**) in pyrite and marcasite ranged in isocubanite-rich, pyrite-, and marcasite-pyrite-rich microfacies. The box encloses the interquartile range with median displayed as a line. The vertical lines extending outside of the box mark the minimum and maximum element concentrations encountered. Outliers are plotted as single points.

Co and Ni: In pyrite, the Co and Ni contents decrease from 2400 to 0.2 ppm passing from isocubanite-rich to marcasite-rich microfacies (Figure 10). Isocubanite, wurtzite, subhedral, and euhedral varieties of pyrite-3 are the main hosts for high concentrations of Co and Ni. The fine-grained pyrite of pyrite-wurtzite-isocubanite microfacies are also enriched in Co and Ni. In contrast, fine-grained pyrite-1,2, framboidal pyrite-1, and oscillatory-zoned pyrite-2 of pyrite-rich microfacies have low Co and Ni as well as possible precursors as greigite and pyrrhotite. It is suggested that these pyrite varieties were formed by low-temperature fluids close to seafloor conditions. Very low concentrations of Co and Ni are found in marcasite, especially, their anhedral and subhedral varieties. Low-temperature conditions (<240 °C) are favorable for marcasite growth [39]. The spongy and subhedral pyrite of marcasite-pyrite microfacies are enriched in Co. Both these pyrite varieties are part of diffuser conduits, probably formed in mid-temperature conditions, whereas marcasite comprises the outer wall of the diffuser near to cold seawater.

In the same assemblages, Co/Ni ratios change from 100 to 0.01 (Figure 3). Pyrite of each microfacies has its own characteristic range of Co/Ni ratios. The highest Co/Ni ratios (100–9) are typical of pyrite-3, isocubanite-pyrite, and pyrite-wurtzite-isocubanite microfacies. In pyrite of pyrite-rich microfacies-196, the Co/Ni ratio mostly varies from 30 to 0.5 with rare exception. The single Co/Ni ratio of 2.8 was detected for greigite, which is one of the precursors of fine-grained pyrite of microfacies-196. In contrast, pyrite of pyrite-rich microfacies-195 formed mostly after pyrrhotite, and the Co/Ni ratios have lower

values (0.9–0.01). These values are characteristic of sedimentary pyrite (e.g., framboidal) formed by diagenetic processes (e.g., [38]). The same range of Co/Ni values is detected for hydrothermal pyrrhotite, which is the precursor for the pyrite of the microfacies-195. There seems to be a correlation between Co/Ni ratios in precursors and pyrite. However, the lack of LA-ICM-MS data for mackinawite and other precursors prevents verification of this hypothesis at this time. Moreover, in marcasite-pyrite facies, pseudomorphs of pyrite after pyrrhotite have high Co/Ni (>1), whereas adjacent marcasite has Co/Ni ratio values less than 1 (Figure 9). Temperature dependence of the Co/Ni ratio could be suggested as the cause for this case.

Many previous investigations [54] indicate that Ni and Co are commonly lattice bound in the structure of pyrite. Ni and Co are temperature-sensitive elements, which are typically enriched in chimney sulfides that precipitate at high temperatures [4,18,19,28,55,56]. Thus, low Cu, Co, and Ni contents in pyrite-rich microfacies indicate a generally low temperature for the fluid. The moderate temperature and less reduced conditions result in precipitation of cobaltite and glaucodot rather than the substitution of Co and Ni in pyrite [4,57]. These minerals were found in the ores of Pobeda vent site [34,35]. Temperature is only one parameter, which controls the solubility of Co and Ni [44]. Depletion in salinity due to phase separation may be another reason for the low Co and Ni contents [19]. Colloform pyrite displays higher concentrations of Co and a Co/Ni ratio > 10 in black smokers from ultramafic- and basaltic-hosted vent sites. Colloform pyrite in modern low-temperature clear smokers from any geological settings has very low contents of Co and Ni and Co/Ni ratio of <1 [20]. Thus, the Co and Ni contents in pyrite are a function of physicochemical parameters of the fluid rather than a reflection of the host rock composition [19]. High contents of Co could also be a proxy for a relatively immature hydrothermal system as calculated by the model of seawater interaction with ultramafites and basalts at 300 °C [45,53].

Zn, As, Sb, and Sn: The contents of Zn are very low in pyrite-3 of isocubanite-pyrite microfacies. The Zn concentrations attain a maximum as wurtzite microinclusions in fine-grained pyrite aggregates of the pyrite–wurtzite-isocubanite microfacies. Minor microinclusions of wurtzite and sphalerite provide less Zn in pyrite of the pyrite-rich microfacies-196 and -195. Variations of Zn contents increase in euhedral pyrite of microfacies-197. Zinc shows flat as well as a spikey concentration patterns with time in LA-ICP-MS depth profiles, most likely reflecting the presence of microparticles of sphalerite [19]. The concentrations of Zn are very low in marcasite-pyrite microfacies-107-10 where sphalerite microinclusions have not been found.

Abundance of wurtzite in pyrite-wurtzite-isocubanite microfacies could be explained on the basis of a hydrothermal fluid-seawater mixing model (e.g., [13]). This model predicts remobilization of Zn at intermediate temperatures (275–325 °C) due to decrease in pH of the fluid, and reprecipitation of ZnS at lower temperatures as continued seawater entrainment gradually raises the pH. In Pobeda hydrothermal fields, the lack of wurtzite and sphalerite in pyrite-rich and marcasite-pyrite microfacies is likely caused by low initial temperature of the hydrothermal mineralization.

As^{3+} and Sb^{3+} can be involved in the coupled substitution of Tl^{+} and Au^{+} for $2Fe^{2+}$ in pyrite (e.g., [26]) and sphalerite [58]. The correlation between As and Sb, as well as Cu and Zn, could be attributed to sulfosalt microinclusions [18]. In Pobeda hydrothermal fields, pyrite of all microfacies demonstrates a positive correlation between Sb and As, As >> Sb, which may partly reflect the presence of microinclusions of invisible tennantite. However, microscopic inclusions of tennantite are rare in sulfides from the MOR [59], and they were not found in Pobeda hydrothermal fields [35] where excess of As relative to Cu and absence of As-Cu-positive correlation could be mostly a result of lattice substitution in the pyrite and marcasite or occurrence as cobaltite that was found in Pobeda vent sites [34,35]. The As concentration decreases also with increase of crystal sizes of pyrite and marcasite. Obviously, this element is expelled from pyrite during recrystallization from porous to massive microtextures (e.g., [18]). In other MS systems, this involves the formation of arsenopyrite (e.g., [60]).

In Pobeda massive sulfides, in addition to As and Sb, wurtzite also has elevated contents of Sn. The Sn, As, and Sb profiles are nearly concordant with Zn profiles, consistent with a decrease in the amount of ZnS microinclusions (Figure 11). The microinclusions of wurtzite are found in pyrite-2 of pyrite microfacies-196 where maximum of Sn is detected (Figure 11d). The high Sn contents are a specific feature of medium- to high-temperature sulfides from volcanic massive sulfide (VMS) deposits [44]. The highest bulk Sn concentrations have been found in sphalerite and isocubanite-chalcopyrite of modern and ancient massive sulfide deposits associated with ultramafic rocks [20,61]. In the modern ocean, sulfide deposits formed on basalts have relatively low Sn concentrations (<92 ppm, [62]). The chimneys from felsic-hosted modern SMS and ancient VMS deposits have much lower Sn contents, except for ancient deposits associated with black shales [20]. The reasons for Sn enrichment are still unclear. Progressive Sn input from magmatic hydrothermal fluids was suggested for some VMS deposits [43,44]. Enhanced concentration of Sn in sphalerite and a good correlation between Sn and Cu imply a substitution mechanism such as suggested elsewhere [58,63]. However, the manner of the substitutions is difficult to validate without evidence for the valence state of Sn in sphalerite. At 250 °C, reduced acid fluids are suitable for the transport of $SnCl_2$ [44]. Substitution of Sn^{2+} for Zn^{2+} is expected under strong reducing conditions [4]. Probably, low redox potential and variable conductive cooling are other important factors for Sn^{2+} enrichment in hydrothermal fluids emanating from diffuse clear smokers, where mixing with oxygenated seawater is restricted. This is consistent with high Sn contents in chimneys with widespread presence of Fe- and Co-rich sphalerite, isocubanite, and pseudomorphic pyrite after pyrrhotite. In general, ultramafics provide reducing conditions favorable for Sn^{2+} saturation in hydrothermal fluids [20]. This scenario is probably realized in the Pobeda hydrothermal system.

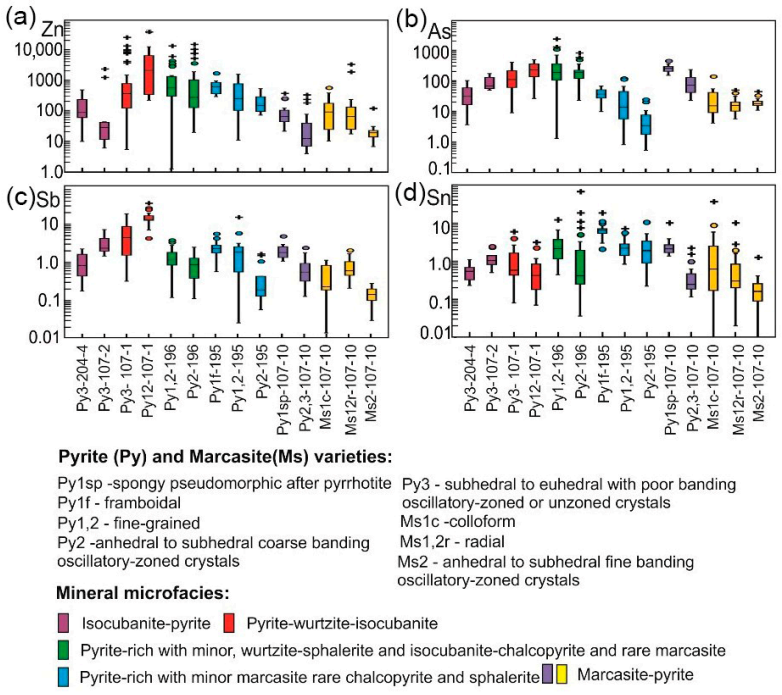

Figure 11. Whisker-and-box plots for the moderate temperature association of elements Zn (**a**), As (**b**), Sb (**c**), and Sn (**d**) in pyrite and marcasite ranged in isocubanite-rich to pyrite and marcasite-pyrite rich microfacies. The box encloses the interquartile range with median displayed as a line. The vertical lines extending outside of the box mark the minimum and maximum element concentrations encountered. Outliers are plotted as single points.

Pb, Tl, Ag, Au, and Mn: In the Pobeda ores, pyrite varieties have low contents of Pb, which are typical of sulfides of serpentinite- and basalt-hosted vent sites in the MOR (e.g., [20]). In the pyrite,

Pb contents increase in the range from isocubanite-pyrite to pyrite-wurtzite-isocubanite facies up to a maximum in fine-grained varieties (Figure 12). The boxplot profiles of Pb and Ag are concordant. On the contrary, in the range from pyrite to marcasite-pyrite microfacies, Pb contents decrease to a minimum in marcasite-2. It was suggested that Pb^{2+} is least likely to be incorporated into the pyrite crystal lattice because of its large ionic radius, and Pb is mainly present as microinclusions of galena or Pb-bearing sulfosalts [26]. In our case, the interquartile ranges (IQR) could be considered as indicators of the pyrite and marcasite crystallization speed. It is inferred that narrow intervals of IQR calculated for Pb, Ag, and Tl indicate a fast crystallization of pyrite, in contrast to slowly grown oscillatory-zoned pyrite (Figure 12a–c).

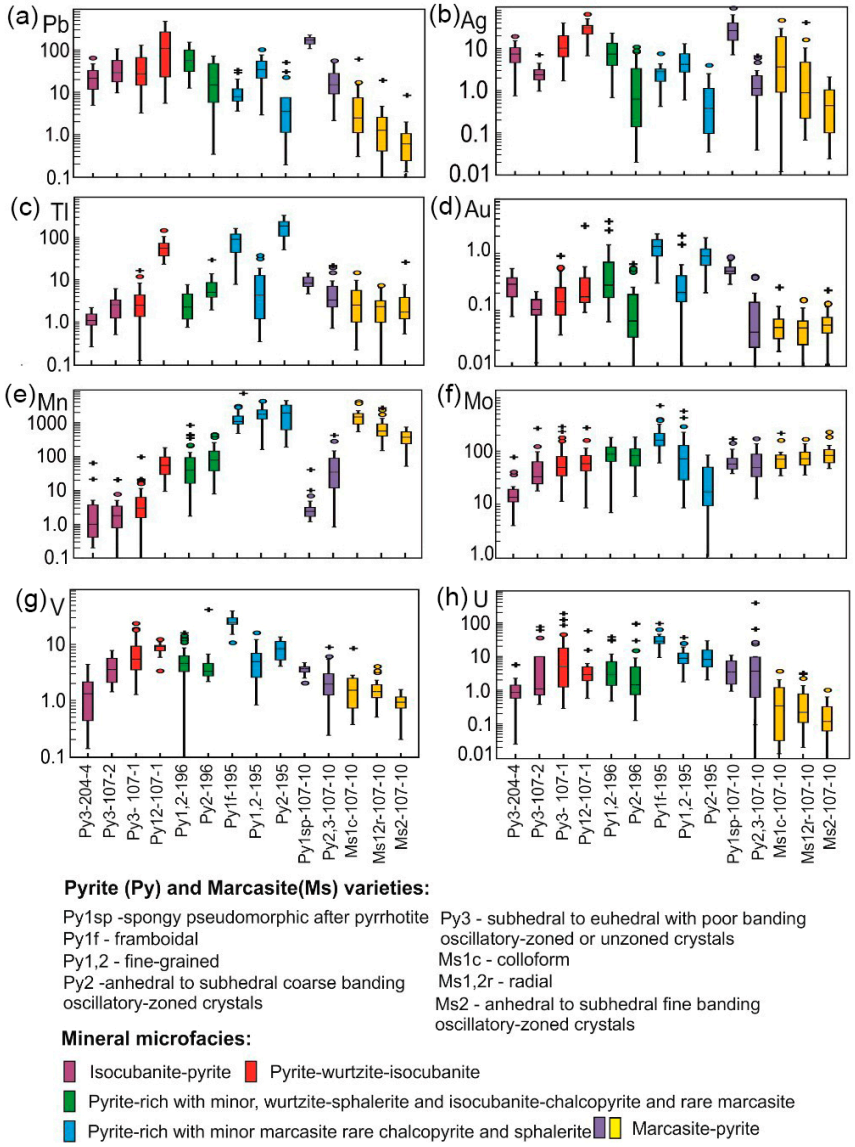

Figure 12. Whisker-and-box plots for the low-temperature (Pb (**a**), Ag (**b**), Tl (**c**), Au (**d**), and Mn (**e**)) and seawater-derived (Mo (**f**), V (**g**), and U (**h**)) association of elements in pyrite and marcasite ranged in isocubanite-rich to pyrite and marcasite-pyrite rich microfacies. The box encloses the interquartile range with median displayed as a line. The vertical lines extending outside of the box mark the minimum and maximum element concentrations encountered. Outliers are plotted as single points.

The positive correlations of Pb and Ag are typical for pyrite of all microfacies studied. The associations of Pb and Ag with Bi or Sb are also common. These elements are likely hosted by nanoinclusions of galena [13] or Pb-Sb-Ag-sulfosalts [11]. Well-known substitutions in galena probably

follow the substitution: $2Pb^{2+} = Ag^{+} + Bi^{3+}$ and $2Pb^{2+} = Ag^{+} + Sb^{3+}$ [37]. In the boxplot, Ag shows two maximums of concentration (Figure 12). These data reflect different aqueous complexing of Ag at different temperatures (e.g., [26,47]).

The highest contents of Tl, Sb, and Pb are typical of fine-grained pyrite in comparison to crystalline pyrite varieties. The boxplot for Tl is comparable with those for Pb, Sb, and Ag (Figure 12a–c). Thallium is likely incorporated into galena dispersed in colloform pyrite via the coupled substitution: $Tl^{+} + (Bi, Sb)^{3+} \leftrightarrow 2Pb^{2+}$ [37]. Probably, this manner of substitution occurs in fine-grained pyrite of pyrite-wurtzite-isocubanite microfacies. Thallium could also be involved in nonstoichiometric substitution in the lattice of pyrite [43].

In the diagram Mn-Ni, the distribution of marcasite is different to typical colloform pyrite that is enriched in Tl and Mn in the outer walls of modern and ancient chimneys [20]. In the diagram Se-Mo, marcasite is characterized by low contents of Se typical of clear smokers [20]. The correlation of Tl with Mn infers coeval growth of pyrite with Mn hydroxides enriched in Tl. The Tl concentration in Mn nodules attains 100 ppm [64]. Mn and Tl higher concentrations are probably linked to low-temperature precipitation of Tl-rich Mn-hydroxides together with sooty, colloform, or fine-grained Fe-sulfides [4]. The Mn adsorption on surfaces of low-temperature immature pyrite and marcasite provides evidence of the greatest exposure of these minerals to seawater in comparison to other pyrite varieties [26].

Framboidal and coarse-zoned pyrite-2 of microfacies 195 are hosts of abundant Tl and As. Monovalent Tl^{+} and trivalent As^{3+} may participate with coupled substitutions for two Fe^{2+} cations [43]. In some cases, the correlation of Tl with Zn suggests well-known incorporation of Tl in wurtzite in the following manner: $Tl^{+} + Ga^{3+} = 2Zn^{2+}$ [26]. The content of Ga attains 163.8 ppm in wurtzite of isocubanite-wurtzite-pyrite microfacies.

The strong positive correlation of Tl with Au suggests coupled incorporation of this elements in framboidal and oscillatory zoned pyrite varieties. However, rare native gold was found in the ores of Pobeda hydrothermal fields [35].

U, V, and Mo: These elements display boxplot profiles similar to those of elements regarded to be of the low-temperature association (Figure 12). The concentrations of these elements increase in pyrite in the range from high-temperature isocubanite-pyrite to middle-temperature pyrite-wurtzite-isocubanite microfacies.

High-temperature pyrites have elevated contents of Mo. In high-temperature pyrite, Mo^{2+} as well as Co^{2+} and Ni^{2+} may directly substitute for Fe^{2+} in pyrite (e.g., [4,26]). The maximum Mo, V, and U contents are detected in the framboidal pyrite. These elements may be adsorbed from seawater during mackinawite transformation to framboidal pyrite. Their contents decrease in the range from framboidal to euhedral pyrite within microfacies-195. High flat levels of Mo are detected in pyrite and marcasite of microfacies-107-10. Marcasite is a typical host for Mo [26]. Molybdenum occurs in ocean water as redox-sensitive oxyanions [64–67]. In Pobeda ore microfacies, the amount of Mo is much less in euhedral pyrite. The molybdate ions are converted into reactive thiomolybdate species and are subsequently incorporated into pyrite and marcasite by interaction with FeS and/or H_2S in sulfidic conditions of sediment pore waters [10,68–70].

Molybdenum has a significant correlation with U and less with V and Mn. This relates to the strong redox behavior of these elements and their source from seawater (e.g., [26,71]). Circulation of seawater through basaltic crust results in quantitative extraction of U, and thus, hydrothermal fluids are essentially free of U [72] as well as of V that mimics U [12]. These elements may be concentrated at the oxic–postoxic boundary of organic-rich sediments [73] or on the surface of sulfide sediments where U and V are concentrated by an efficient redox trap mechanism [12]. The Pobeda ore deposits yields a maximum average of U (24.86 ppm) in comparison to other massive sulfide deposits (mean 3.53 ppm) of the Mid-Atlantic Ridge [23]. The similar diagenetic processes of U accumulation as uraninite in modern and ancient Fe-oxyhydroxide sediments were the result of U fixation from seawater during the oxidation of sulfide minerals. Uraninite in gossanites is mainly deposited from diagenetic pore fluids, which circulated in the sulfide-hyaloclast-carbonate sediments [23]. Pyrite surfaces are thought

to have strong reducing capabilities, which caused fixation of the very low solubility redox-sensitive elements such as V and U, ensuring that they are retained by the pyrite [12]. Experimental studies of interaction between U (VI) in solution and sulfide mineral surface [74] provide evidence for sorption and reduction of U (VI) to uraninite on those surfaces.

The contents of V and U decease in profile from pyrite to marcasite. Probably, low-pH conditions of marcasite growth (pH < 4.5) [39] are not favorable for U and V adsorption on marcasite surfaces.

6. Conclusions

In the Pobeda SMS deposits, the main mineral microfacies are: isocubanite-pyrite → pyrite-wurtzite-isocubanite → pyrite with minor isocubanite, chalcopyrite, wurtzite-sphalerite, and rare marcasite → pyrite with rare chalcopyrite and sphalerite and subordinate marcasite → marcasite-pyrite. This sequence reflects the transition from feeder zone facies to seafloor diffuser facies. It is suggested that temperatures of mineralization decreased in the same direction.

In the Pobeda deposits, the precursors of pyrite are greigite, pyrrhotite, and mackinawite. Several pyrite varieties are recognized in these microfacies. Subhedral and euhedral unzoned pyrite-3 crystals are predominant in high-temperature isocubanite-pyrite microfacies. There are no relicts of fine-grained pyrite except residual holes in atoll-textured aggregates. Poor zonation is retained in subhedral and euhedral pyrite-3 of mid-temperature pyrite wurtzite-isocubanite microfacies. Coarse-grained pseudomorphs of pyrite after pyrrhotite crystals and later fine-grained pyrite occur in these microfacies. Intermediate from mid-to-low-temperature pyrite microfacies contains abundant fine-grained pyrite-1,2 and coarse-grained pyrite-2. Despite coarse and fine banding, oscillatory-zoned pyrite-2, fine-grained pseudomorphs after pyrrhotite crystals, and framboidal pyrite are widespread in low-temperature pyrite microfacies. In marcasite-pyrite microfacies, spongy pyrite replacing pyrrhotite crystals and sooty colloform-like marcasite occurs in addition to anhedral and subhedral pyrite and marcasite masses with relic framboidal pyrite.

The trace elements of Pobeda SMS deposit are subdivided into four associations: (1) high temperature—Cu, Se, Te, Bi, Co, and Ni; (2) mid temperature—Zn, As, Sb, and Sn; (3) low temperature—Pb, Sb, Ag, Bi, Au, Tl, and Mn; and (4) seawater—U, V, Mo, and Ni. The trend of Co/Ni ratio values indicates a change from hydrothermal to hydrothermal-diagenetic crystallization of the pyrite. The concentration of the high-temperature group of elements (Cu, Co, Ni, Se, Bi, and Te) and the Co/Ni ratios generally decreases from unzoned euhedral pyrite to marcasite in the same assemblage. The concentrations of mid- and low-temperature (Zn, As, Sb, Pb, Ag, and Tl) elements decrease with increasing crystal sizes of pyrite and marcasite. Coarse banded oscillatory-zoned pyrite crystals contain higher concentrations of Mn especially compared to unzoned euhedral pyrite varieties. Framboidal pyrite hosts the maximum concentration of Au and seawater-derived elements (Mo, U, and V).

We hope, the results of this investigation can be used to better interpret the paragenesis and deposition temperatures of ancient massive sulfide deposits.

Supplementary Materials: The following are available online at http://www.mdpi.com/2075-163X/10/7/622/s1, Table S1: Trace element contents in the pyrite-chalcopyrite crusts, Table S2: Trace element concentration in sulfides of the pyrite-sphalerite-chalcopyrite crusts, Table S3: Trace element contents in sulfides of third style pyrite crusts, Table S4: Trace element concentration in pyrrhotite and varieties of pyrite of microfacies-195, Table S5: Trace element contents in pyrite varieties of marcasite-pyrite microfacies.

Author Contributions: V.V.M. interpreted results and wrote the text; G.C. and A.F. carried out the sampling; D.A.A. performed LA-ICP-MS analyses; A.T. and V.K. performed the microprobe analyses; and R.R.L. revised the manuscript. All authors have read and agreed to the published version of the manuscript.

Funding: This research was funded by project 18-05-00861 "Reconstruction of the history of ocean hydrothermal ore genesis on the basis of joint analysis of sulfide ores and metal-bearing sediments: Pobeda ore cluster, Mid-Atlantic Ridge" and was partly supported by Ministry of Science and Higher Education (State Contract no. AAAA-A19-119061790049-3).

Acknowledgments: The authors are sincerely grateful to Victor Beltenev, the team, and all participants of the R.V. Logachev Cruise 37 for the vital assistance.

Conflicts of Interest: The authors declare no conflicts of interest.

References

1. Large, R.R.; Maslennikov, V.V.; Robert, F.; Danyushevsky, L.V. Multistage sedimentary and metamorphic origin of pyrite and gold in the Giant Sukhoi Log deposit, Lena Gold Province, Russia. *Econ. Geol.* **2007**, *102*, 1233–1267. [CrossRef]
2. Large, R.R.; Danyushevsky, L.; Hollit, C.; Maslennikov, V.; Meffre, S.; Gilbert, S.; Bull, S.; Scott, R.; Emsbo, P.; Thomas, H.; et al. Gold and trace element zonation in pyrite using a laser imaging technique: Implications for the timing of gold in orogenic and Carlin-style sediment-hosted deposits. *Econ. Geol.* **2009**, *104*, 635–668.
3. Large, R.R.; Gregory, D.D.; Steadman, J.A.; Tompkins, A.G.; Lounjeva, E.; Danyushevsky, L.D.; Halpin, J.A.; Maslennikov, V.V.; Sack, P.J.; Mukherjee, I.; et al. Gold in the oceans through time. *Earth Planet. Scie. Lett.* **2015**, *428*, 139–150. [CrossRef]
4. Maslennikov, V.V.; Maslennikova, S.P.; Large, R.R.; Danyushevsky, L.V. Study of trace element zonation in vent chimneys from the Silurian Yaman-Kasy VHMS (the Southern Urals, Russia) using laser ablation inductively coupled plasma mass spectrometry (LA-ICPMS). *Econ. Geol.* **2009**, *104*, 1111–1141. [CrossRef]
5. Thomas, H.V.; Large, R.R.; Bull, S.W.; Maslennikov, V.V.; Berry, R.F.; Fraser, R.; Froud, S.; Moye, R. Pyrite and pyrrhotite textures and composition in sedimentary rocks, laminated quartz veins, and gold reefs, at Bendigo Mine, Australia: Insights for ore genesis. *Econ. Geol.* **2011**, *105*, 1–40. [CrossRef]
6. Revan, M.K.; Genc, Y.; Maslennikov, V.V.; Ünlü, T.; Delibas, O.; Hamzaçebi, S. Original finding on the ore-bearing facies of volcanogenic massive sulfide deposits in the Eastern Black Sea region (NE Turkey). *Bull. Miner. Res. Explor.* **2013**, *147*, 73–89.
7. Steadman, J.A.; Large, R.R.; Meffre, S.; Olin, P.H.; Danyushevsky, L.V.; Gregory, D.D.; Belousov, I.; Lounejeva, E.; Ireland, T.R.; Holden, P. Synsedimentary to early diagenetic gold in black shale-hosted pyrite nodules at the Golden Mile deposit, Kalgoorlie, Western Australia. *Econ. Geol.* **2015**, *110*, 1157–1191. [CrossRef]
8. Mukherjee, I.; Large, R. Aplication of pyrite trace element chemistry to exploration for SEDEX type Zn-Pb deposits: McArthur Basin, Nothern Territory, Australia. *Ore Geol. Rev.* **2017**, *81*, 1249–1270. [CrossRef]
9. Belousov, I.; Large, R.R.; Meffre, S.; Danyushevsky, L.V.; Steadman, J.; Beardsmore, T. Pyrite compositions from VHMS and orogenic Au deposits in the Yilgarn Craton, Western Australia: Implications for gold and copper exploration. *Ore Geol. Rev.* **2016**, *79*, 474–499. [CrossRef]
10. Large, R.R.; Halpin, J.A.; Danyushevsky, L.V.; Maslennikov, V.V.; Bull, S.W.; Long, J.A.; Gregory, D.D.; Lounejeva, E.; Lyons, T.W.; Sack, P.J.; et al. Trace element content of sedimentary pyrite as a new proxy for deep-time ocean–atmosphere evolution. *Earth Planet. Sci. Lett.* **2014**, *389*, 209–220. [CrossRef]
11. Halbach, P.; Blum, N.; Münch, U.; Plüger, W.; Garbe-Schönberg, D.; Zimmer, M. Formation and decay of a modern massive sulfide deposit in the Indian Ocean. *Miner. Deposita.* **1998**, *33*, 302–309. [CrossRef]
12. Butler, I.B.; Nesbitt, R.W. Trace element distributions in the chalcopyrite wall of a black smoker chimney; insights from laser ablation inductively-coupled plasma mass spectrometry (LA-ICP-MS). *Earth Planet. Sci. Lett.* **1999**, *167*, 335–345. [CrossRef]
13. Houghton, J.L.; Shanks, W.C.; Seyfried, W.E., Jr. Massive sulfide deposition and trace element remobilization in the Middle Valley sediment-hosted hydrothermal system, northern Juan de Fuca Ridge. *Geochim. Cosmochim. Acta* **2004**, *68*, 2863–2873. [CrossRef]
14. Bogdanov, Y.A.; Lein, A.Y.; Maslennikov, V.V.; Syaoli, L.; Ulyanov, A.A. Mineralogical-geochemical features of sulfide ores from the Broken Spur hydrothermal field. *Oceanology.* **2008**, *48*, 679–700. [CrossRef]
15. Lein, A.Y.; Bogdanov, Y.A.; Maslennikov, V.V.; Li, S.; Ulyanova, N.V.; Maslennikova, S.P.; Ulyanov, A.A. Sulfide minerals in the Menez Gwen nonmetallic hydrothermal field (Mid-Atlantic Ridge). *Lithol. Miner. Resour.* **2010**, *45*, 305–323. [CrossRef]
16. Li, B.; Yang, Y.; Shi, X.; Ye, J.; Gao, J.; Zhu, A.; Shao, M. Characteristics of a ridge-transform inside corner intersection and associated mafic-hosted seafloor hydrothermal field (14.0°S, Mid-Atlantic Ridge). *Mar. Geophys. Res.* **2014**, *35*, 55–68. [CrossRef]

17. Melekestseva, I.Y.; Tret'yakov, G.A.; Nimis, P.; Yuminov, A.M.; Maslennikov, V.V.; Maslennikova, S.P.; Kotlyarov, V.A.; Beltenev, V.E.; Danyushevsky, L.V.; Large, R. Barite-rich massive sulfides from the Semenov-1 hydrothermal field (Mid-Atlantic Ridge, 13°30.87′N): Evidence for phase separation and magmatic input. *Mar. Geol.* **2014**, *349*, 37–54. [CrossRef]
18. Wohlgemuth-Ueberwasser, C.C.; Viljoen, F.; Petersen, S.; Vorster, C. Distribution and solubility limits of trace elements in hydrothermal black smoker sulfides: An in-situ LA-ICP-MS study. *Geochim. Cosmochim. Acta* **2015**, *159*, 16–41. [CrossRef]
19. Keith, M.; Häckel, F.; Haase, K.M.; Schwarz-Schampera, U.; Klend, R. Trace elements systematics of pyrite from submarine hydrothermal vents. *Ore Geol. Rev.* **2016**, *72*, 728–745. [CrossRef]
20. Maslennikov, V.V.; Maslennikova, S.P.; Ayupova, N.R.; Zaykov, V.V.; Tseluyko, A.S.; Melekestseva, I.Y.; Large, R.R.; Danyushevsky, L.V.; Herrington, R.J.; Lein, A.T.; et al. Chimneys in Paleozoic massive sulfide mounds of the Urals VMS deposits: Mineral and trace element comparison with modern black, grey, white and clear smokers. *Ore Geol. Rev.* **2017**, *85*, 64–106. [CrossRef]
21. Melekestseva, I.Y.; Maslennikov, V.V.; Tret'yakov, G.A.; Nimis, P.; Beltenev, V.E.; Rozhdestvenskaya, I.I.; Maslennikova, S.P.; Belogub, E.V.; Danyushevsky, L.; Large, R.; et al. Gold- and Silver-Rich Massive Sulphides from the Semenov-2 Hydrothermal Field, 13°31.13′ N, Mid-Atlantic Ridge: A Case of Magmatic Contribution? *Econ. Geol.* **2017**, *112*, 741–773. [CrossRef]
22. Wang, H.; He, M.; Chen, B.; Hu, B. Advances in ICP-MS-based techniques for trace elements and their species analysis in cells. *J. Anal. At. Spectrom.* **2017**, *32*, 1650–1659. [CrossRef]
23. Ayupova, N.R.; Melekestseva, I.Y.; Maslennikov, V.V.; Tseluyko, A.S.; Blinov, I.A.; Beltenev, V.E. Uranium accumulation in modern and ancient Fe-oxide sediments: Examples from the Ashadze-2 hydrothermal sulfide field (Mid-Atlantic Ridge) and Yubileynoe massive sulfide deposit (South Urals, Russia). *Sediment. Geol.* **2018**, *367*, 167–174. [CrossRef]
24. Dekov, V.M.; Garbe-Schonberg, D.; Kamenov, G.D.; Gueguen, B.; Bayon, G.; Bindi, L.; Asael, D.; Fouquet, Y. Redox changes in a seafloor hydrothermal system recorded in hematite-chalcopyrite chimneys. *Chem. Geol.* **2018**, *483*, 351–371. [CrossRef]
25. Yuan, B.; Hongjun, Y.; Yang, Y.; Zhao, Y.; Yang, J.; Xu, Y.; Lin, Z.; Tang, X. Zone refinement related to the mineralization process as evidenced by mineralogy and element geochemistry in a chimney fragment from the Southwest Indian Ridge at 49.6° E. *Chem. Geol.* **2018**, *482*, 46–60. [CrossRef]
26. Grant, H.L.J.; Hannington, M.D.; Petersen, S.; Frische, M.; Fuchs, S.H. Constraints on the behavior of trace elements in the actively-forming TAG deposit, Mid-Atlantic Ridge, based on LA-ICP-MS analyses of pyrite. *Chem. Geol.* **2018**, *498*, 45–71. [CrossRef]
27. Melekestseva, I.; Maslennikov, V.V.; Safina, N.P.; Nimis, P.; Maslennikova, S.P.; Beltenev, V.; Rozhdestvenskaya, I.; Danyushevsky, L.V.; Large, R.; Artemyev, D.A.; et al. Sulfide breccias from the Semenov-3 hydrothermal field, Mid-Atlantic Ridge: Authigenic mineral formation and trace element pattern. *Minerals* **2018**, *8*, 321. [CrossRef]
28. Meng, X.; Li, X.; Chu, F.; Zhu, J.; Lei, J.; Li, Z.; Wang, H.; Chen, L.; Zhu, Z. Trace element and sulfur isotope compositions for pyrite across the mineralization zones of a sulfide chimney from the East Pacific Rise (1–2° S). *Ore Geol. Rev.* **2020**, *116*, 1–15. [CrossRef]
29. Klaus, K.E.; Neuendorf, J.P.; Mehl, Jr.; Jackson, J.A. Glossary of Geology. *Am. Geol. Inst. Alex. Va.* **2005**, 779.
30. Flügel, E. Microfacies of Carbonate Rocks (Analysis, Interpretation and Application. Springer: Berlin/Hedelberg, Germany, 2004; 976p.
31. Beltenev, V.E.; Narkevsky, E.V.; Dobretsova, I.G.; Gablina, I.F.; Galkin, S.V.; Molodtsova, T.N.; Layba, A.A. The results of Professor Logatchev-37 cruise, MAR. In Proceedings of the XXI International Scientific Conference (School) on Marine Geology, Moscow, Russia, 16–20 November 2015; GEOS: Moscow, Russia, 2015; pp. 126–128. (In Russian).
32. Beltenev, V.E.; Rozhdestvenskay, I.I.; Samsonov, I.K. *Exploration work on the Russian exploration area in the Atlantic Ocean with an estimate forecast resources of GPS of categories P2 and P3 in blocks 31-45. Report of Professor Logachev-37 cruise; Lomonosov, Russia*; PMGRE: Saint Petersburg, Russia, 2016. (In Russian)
33. Cherkashov, G.; Kuznetsov, V.; Kuksa, K.; Tabuns, E.; Maksimov, F.; Bel'tenev, V. Sulfide geochronology along the Northern Equatorial Mid-Atlantic Ridge. *Ore Geol. Rev.* **2017**, *87*, 147–154. [CrossRef]

34. Amplieva, E.E.; Bortnikov, N.S.; Kovalchuk, E.V.; Beltenev, V.E. The Pobeda modern submarine hydrothermal sulfide edifice cluster (Mid-Atlantic Ridge, 17°08′ N): Mineralogy and chemical composition. In Proceedings of the 14th SGA Biennial Meeting. Mineral Resources to Discover, Quebec Citi, QC, Canada, 20–23 August 2017; Volume 1–4, pp. 649–652.
35. Gablina, I.F.; Dobretzova, I.G.; Narkevsky, E.V.; Maksimov, F.E.; Kuznetsov, V.Y. Specific features of sulfide ores in the Pobeda hydrothermal cluster, Mid-Atlantic rise 17°07′–17°08′ N. *Lithol. Miner. Resour.* **2018**, *53*, 431–454. [CrossRef]
36. Smirnov, V.I. *Correlation Methods in Paragenetic Analysis*; Nedra Publishers: Moscow, Russia, 1981; p. 174. (In Russian)
37. George, L.L.; Ciik, N.J.; Ciobanu, C.I.; Wade, B.P. Trace and minor elements in galena: A reconnaissance LA-ICP-MS study. *Am. Mineral.* **2015**, *100*, 548–569. [CrossRef]
38. Rickard, D. *Sulfidic Sediments and Sedimentary Rocks, Developments in Sedimentology*; Elsevier: Amsterdam, The Netherlands, 2012; p. 801.
39. Murowchick, J.B.; Barnes, H.L. Marcasite precipitation from hydrothermal solutions. *Geochim. Cosmochim. Acta* **1986**, *50*, 2615–2629. [CrossRef]
40. Xia, F.; Detitius, A.P.; Brugger, J.; Pearse, M.A. The mechanism and kinetics of the transformation from marcasite to pyrite: In situ and ex situ experiments and geological implications. *Contrib. Mineral. Petrol.* **2020**, *175*, 1–25.
41. Auclair, M.; Fouquet, Y.; Bohn, M. Distribution of selenium in high-temperature hydrothermal sulfide deposits at 13° North, East Pacific Rise. *Canad. Mineral.* **1987**, *25*, 577–587.
42. Halbach, P.E.; Fouquet, Y.; Herzig, P. Mineralization and compositional patterns in deep-sea hydrothermal systems. In *Energy and Mass Transfer in Marine Hydrothermal*; Halbach, P.E., Tunnicliffe, V., Hein, J.R., Eds.; Dahlem Univ. Press: Berlin, Germany, 2003; pp. 85–122.
43. Huston, D.L.; Sie, S.H.; Sutter, G.F.; Cook, D.R.; Both, R.A. Trace elements in sulfide minerals from Eastern Australian volcanic-hosted massive sulfide deposits. Part I, proton microprobe analyses of pyrite, chalcopyrite, and sphalerite, and Part II. Selenium levels in pyrite. comparison with δS34 values and implication for the source of sulfur in volcanogenic hydrothermal systems. *Econ. Geol.* **1995**, *90*, 1167–1196.
44. Hannington, M.D.; Bleeker, W.; Kjarsgaard, I. Sulfide mineralogy, geochemistry, and ore genesis of the Kidd Creek Deposit: Part II. The bornite zone. In *The giant Kidd Creek Volcanogenic Massive Sulfide Deposit, Western Abitibi Subprovince, Canada*; Hannington, M.D., Barrie, C.T., Eds.; Economic Geology Monograph: Ottawa, ON, Canada, 1999; Volume 10, pp. 225–267.
45. Toffolo, T.; Nimis, P.; Tret'yakov, G.A.; Melekestseva, I.Y.; Beltenev, V.E. Seafloor massive sulfides from mid-ocean ridges: Exploring the causes of their geochemical variability with multivariate analysis. *Earth-Sci. Rev.* **2020**, *102958*. [CrossRef]
46. Urusov, V.S. *Theoretical Crystal Chemistry*; Moscow State University: Moscow, Russia, 1987; p. 275.
47. Hannington, M.; Herzig, P.; Scott, S.; Thompson, G.; Rona, P. Comparative mineralogy and geochemistry of gold-bearing sulfide deposits on the mid-ocean ridges. *Mar. Geol.* **1991**, *101*, 217–248. [CrossRef]
48. Hannington, M.D.; Jonasson, I.R.; Herzig, P.M.; Petersen, S. Physical, chemical processes of sea- floor mineralization at mid-ocean ridges. In *Seafloor Hydrothermal Systems: Physical, Chemical, Biological and Geological Interactions*; Humphris, S.E., Zierenberg, R.A., Mullineaux, L.S., Thomson, R.E., Eds.; Geophisical. Monoraph Series: Washington, DC, USA, 1995; Volume 91, pp. 115–157.
49. Rouxel, O.; Fouquet, Y.; Ludden, J.N. Subsurface processes at the Lucky Strike hydrothermal field, Mid-Atlantic ridge: Evidence from sulfur, selenium, and iron isotopes. *Geochim. Cosmochim. Acta* **2004**, *68*, 2295–2311. [CrossRef]
50. Spooner, E.T.C. Magmatic sulfide volatile interaction as a mechanism for producing chalcofile element enriched, Archean Au-quartz, epitermal Au-Ag and Au-skarn hydrothermal ore fluids. *Ore Geol. Rev.* **1993**, *7*, 359–379. [CrossRef]
51. Berkenbosh, H.A.; De Ronde, C.E.J.; Gemmel, J.B.; McNel, A.W.; Goemann, K. Mineralogy and formation of black smoker chimneys from Brothers submarine volcano, Kermadec arc. *Econ. Geol.* **2012**, *107*, 1613–1633. [CrossRef]
52. Janecky, D.R.; Seyfried, W.F., Jr. Formation of massive sulfide deposits on oceanic ridge crests: Incremental reaction models for mixing between hydrothermal solutions and sea water. *Geochim. Cosmochim. Acta* **1984**, *48*, 2723–2738. [CrossRef]

53. Tret'yakov, G.A. Mineral assemblages and behavior of ore-forming elements at rock-seawater interaction in hydrothermal conditions. *Lithosphere* **2015**, *6*, 142–147. (In Russian)
54. Vaughan, D.J.; Rosso, K.M. Chemical bonding in sulfide minerals. *Rev. Mineral. Geochem.* **2006**, *61*, 231–264. [CrossRef]
55. De Ronde, C.E.J.; Massoth, G.J.; Butterfield, D.A.; Christenson, B.W.; Ishibashi, J.; Ditchburn, R.G.; Hannington, M.D.; Brathwaite, R.L.; Lupton, J.E.; Kamenetsky, V.S.; et al. Submarine hydrothermal activity and gold-rich mineralization at Brothers volcano, Kermadec Arc, New Zealand. *Miner. Depos.* **2011**, *46*, 541–584. [CrossRef]
56. Metz, S.; Trefry, J.H. Chemical and mineralogical influences on concentration of trace metals in hydrothermal fluids. *Geochim. Cosmochim. Acta* **2000**, *64*, 2267–2279. [CrossRef]
57. Maslennikov, V.V.; Maslennikova, S.P.; Large, R.R.; Danyushevsky, L.V.; Herrington, R.J.; Stanley, C.J. Tellurium-bearing minerals in zoned sulfide chimneys from Cu-Zn massive sulfide deposits of the Urals, Russia. *Mineral. Petrol.* **2013**, *107*, 67–99. [CrossRef]
58. Ye, L.; Cook, N.J.; Ciobanu, C.L.; Liu, Y.P.; Zang, Q.; Liu, T.-G.; Gao, W.; Yang, Y.-L.; Danyushevsky, L. Trace elements in sphalerite from base metal deposits in South China: A LA-ICPMS study. *Ore Geol. Rev.* **2011**, *39*, 188–217. [CrossRef]
59. Mozgova, N.N.; Borodaev, B.N.; Yu, S.; Efimov, A.V.; Krasnov, S.G.; Stepanova, T.V.; Samovarov, M.L. Features of the chemical composition of fahlores from hydrothermal deposits of the mid-ocean ridges (MIR construction, TAG field 26° N. of the Mid-Atlantic ridge). *Proc. Russ. Mineral. Soc.* **1995**, *124*, 77–84.
60. Almodovar, G.R.; Yesares, L.; Saez, R.; Toscano, M.; Gonzalez, F.; Pons, J.M. Massive sulfide ores in the Iberian Pyrite Belt: Mineralogical and textural evolution. *Minerals* **2019**, *9*, 653. [CrossRef]
61. Evrard, C.; Fouquet, Y.; Moelo, Y.; Rinnert, E.; Etoubleau, J.; Langlade, J.A. Tin concentration in hydrothermal sulfides related to ultramafic rocks along the Mid-Atlantic Ridge: A mineralogical study. *Eur. J. Miner.* **2015**, *27*, 627–638. [CrossRef]
62. Fouquet, Y.; Cambon, P.; Etoubleau, J.; Charlou, J.L.; Ondréas, H.; Barriga, F.; Cherkashov, G.; Semkova, T.; Poroshina, I.; Bohn, M.; et al. Geodiversity of hydrothermal processes along the mid-atlantic ridge and ultramafic-hosted mineralization: A new type of oceanic Cu-Zn-Co-Au volcanogenic massive sulfide deposit. In *Diversity of Hydrothermal Systems on Slow Spreading Ocean Ridges*; Geophisical. Monoraph Series: Washington, DC, USA, 2010; Volume 188, pp. 321–367.
63. Cook, N.J.; Ciobanu, C.L.; Pring, A.; Skinner, W.; Shimizu, M.; Danyushevsky, L.; Saini-Eidukat, B.; Melcher, F. Trace and minor elements in sphalerite: A LA-ICP-MS study. *Geochim. Cosmochim. Acta* **2009**, *73*, 4761–4791. [CrossRef]
64. Hein, J.R.; Mizell, K.; Koschinsky, A.; Conrad, T.A. Deep-ocean mineral deposits as a source of critical metals for high- and green-technology applications: Comparison with land-based resources. *Ore Geol. Rev.* **2013**, *51*, 1–14. [CrossRef]
65. Minubayeva, Z.; Seward, T.M. Molybdic acid ionisation under hydrothermal conditions to 300 °C. *Geochim. Cosmochim. Acta* **2010**, *74*, 4365–4374. [CrossRef]
66. Wiliams-Jones, A.E.; Migdisov, A.A. Experimental Constraints on the Transport and Deposition of Metals in Ore-Forming Hydrothermal Systems. In *Buiding Exploration Capability for the 21st Century*; Kelley, K.D., Golden, H.C., Eds.; Society of Economic Geologists: Ottawa, ON, Canada, 2014; Volume 18, pp. 77–95.
67. Monecke, T.; Petersen, S.; Hannington, M.D.; Grant, H.; Samson, I.M. The minor element endowment of modern sea-floor massive sulfides and comparison with deposits hosted in ancient volcanic successions. *Econ. Geol.* **2016**, *18*, 245–306.
68. McManus, J.; Berelson, W.B.; Severmann, S.; Poulson, R.L.; Hammond, D.E.; Klinkhammer, G.P.; Holm, C. Molybdenum and uranium geochemistry in continental margin sediments: Paleoproxy potential. *Geochim. Cosmochim. Acta* **2006**, *70*, 4643–4662. [CrossRef]
69. Berner, Z.A.; Puchelt, H.; Nöltner, T.; Kramar, U. Pyrite geochemistry in the Toarcian Posidonia Shale of southwest Germany: Evidence for contrasting trace-element patterns of diagenetic and syngenetic pyrites. *Sedimentology* **2013**, *60*, 548–573. [CrossRef]
70. Helz, G.R.; Vorlicek, T.P. Precipitation of molybdenum from euxinic waters and the role of organic matter. *Chem. Geol.* **2019**, *509*, 178–193. [CrossRef]

71. Sukhanova, A.; Firstova, A.; Stepanova, T.; Cherkashov, G. Uranium in seafloor massive sulfides at the Mid-Atlantic Ridge. In Proceedings of the Sustanable Development of Seabed Mineral Resources: Environment, Regulations and Technologies, UMS 2019 48th Underwater Mining Conference, Sanya, China, 22 September 2019; p. 3.
72. Mills, R.A.; Thomson, J.; Elderfield, H.; Hinton, R.W.; Hyslop, E. Uranium enrichment in metalliferous sediments from the Mid-Atlantic Ridge. *Earth Planet. Sci. Lett.* **1994**, *124*, 35–47. [CrossRef]
73. Thomson, J.; Higgs, N.C.; Croudace, I.W.; Colley, S.; Hydes, D.J. Redox zonation of elements at an oxic/postoxic boundary in deep-sea sediments. *Geochim. Cosmochim. Acta* **1993**, *57*, 579–595. [CrossRef]
74. Wersin, P.; Hochella, M.F., Jr.; Perrson, P.; Redden, G.; Leckie, J.O.; Harris, D.W. Interaction between aqueous uranium (VI) and sulphide minerals: Spectroscopic evidence for sorption and reduction. *Geochim. Cosmochim. Acta* **1994**, *58*, 2829–2844. [CrossRef]